POLITECNICO DI TORINO

Department of Mechanical and Aerospace Engineering

Master's Degree in Aerospace Engineering

Master's Degree Thesis

WIVERN Potential in Revealing Tropical Cyclone Structure and Rapid Intensification

Supervisors

Prof. Alessandro Battaglia

Prof. Fabrizio Stesina

Candidate

Massimiliano Recupero

2024/2025 Academic year

Abstract

This thesis investigates the observational capabilities of the Wind Velocity Radar Nephoscope (WIVERN) mission, recently selected for Phase A studies within ESA Earth Explorer 11 program. The mission aims to address a longstanding gap in the global observation system: the lack of direct measurements of three-dimensional wind fields within clouds, particularly in the context of tropical cyclones.

Unlike conventional remote sensing systems, WIVERN is designed to provide vertically resolved, in-cloud wind observations across an 800 km-wide swath with kilometre-scale horizontal resolution and quasi-daily global coverage. This represents a significant advancement in the ability to monitor storm-scale dynamics from space.

The study explores WIVERN potential in two key aspects of tropical cyclone research: the reconstruction of internal wind structure and the detection of storm rapid intensification. WIVERN-like observations are simulated by applying an end-to-end simulations to high-resolution WRF data of Hurricane Milton (2024).

Results show that WIVERN is able to resolve essential dynamical features such as low-level inflow and outflow layers, upper-level divergence, vertical wind shear and in-cloud circulation within convective anvils. Additionally, in scenarios with close-in-time overpasses, WIVERN demonstrates the ability to capture changes in maximum wind speeds within the cyclone's inner core, enabling the identification of intensification phases.

These findings highlight the mission's potential to improve the global monitoring of tropical cyclones and to improve our understanding of their evolution in a changing climate.

Table of Contents

List of Tables

List of Figures

Acronyms

ADT
Advanced Dvorak Technique

DL
Downshear Left

DR
Downshear Right

ECEF
Earth-Centered Earth-Fixed

ENU
East-North-Up

ERC
Eyewall Replacement Cycle

ESA
European Space Agency

GPM
Global Precipitation Measurement

HLOS
Horizontal Line-Of-Sight

LOS
Line of Sight

LTAN

Local Time of Ascending Node

MCS

Mesoscale Convective System

MCV

Mesoscale Convective Vortex

NASA

National Aeronautics and Space Administration

NHC

National Hurricane Center

NOAA

National Oceanic and Atmospheric Administration

NWP

Numerical Weather Prediction

PIA

Path-Integrated Attenuation

PRF

Pulse Repetition Frequency

RI

Rapid Intensification

RMW

Radius of Maximum Wind

RMS

Root Mean Square

RRTMG

Rapid Radiative Transfer Model for General circulation

RUC

Rapid Update Cycle

SAB

Satellite Analysis Branch

SCR

Signal-to-Clutter Ratio

SNR

Signal-to-Noise Ratio

SSHWS

Saffir–Simpson Hurricane Wind Scale

TAFB

Tropical Analysis and Forecast Branch

TC

Tropical Cyclone

TDR

Tail Doppler Radar

TKE

Turbulent Kinetic Energy

TRMM

Tropical Rainfall Measuring Mission

UL

Upshear Left

UR

Upshear Right

UTC

Coordinated Universal Time

VHT

Vortical Hot Tower

WRF

Weather Research and Forecasting model

YSU

Yonsei University planetary boundary layer scheme

Introduction

Tropical cyclones (TCs) rank among the most powerful and destructive meteorological phenomena on Earth. Their impacts, ranging from devastating winds and torrential rainfall to storm surges, pose a significant threat to coastal populations and infrastructure. Beyond the immediate damage, these storms challenge operational forecasting due to their rapidly evolving internal dynamics and sensitivity to environmental conditions.

In recent decades, the frequency and severity of high-end tropical cyclones have shown signs of increasing, with a notable rise in rapid intensification (RI) events, sudden surges in cyclone strength over short timescales. This trend has been linked to rising sea surface temperatures and a more energetic atmosphere, consistent with the broader effects of anthropogenic climate change (Bhatia et al. 2019; Emanuel 2020). These developments have heightened the urgency of improving monitoring tools and predictive models for extreme weather systems.

A key obstacle in forecasting TC behavior lies in the limited availability of accurate, high-resolution observations within the storm's inner core, the region most critical for determining cyclone intensity and structural evolution. Traditional remote sensing systems, including passive microwave and infrared imagers, provide valuable information on cloud top structure and rainfall but fail to directly resolve the full three-dimensional wind field. While airborne platforms such as dropsondes and Doppler radar flights offer detailed snapshots, they are spatially and temporally constrained.

To address these gaps, Doppler radar systems in space have emerged as a promising avenue for observing storm-scale wind fields in a more comprehensive and operationally useful manner. In particular, the WIVERN (WInd VElocity Radar Nephoscope) mission, recently selected by the European Space Agency for Phase A studies, introduces a novel approach to atmospheric wind profiling (ESA 2025). By employing a conically scanning W-band Doppler radar on a spinning satellite platform, WIVERN aims to deliver simultaneous measurements of reflectivity and line-of-sight winds in precipitating clouds across a wide swath. The mission's unique slant-view geometry enhances its ability to probe deep into convective systems, offering a level of vertical and horizontal detail that nadir-looking systems cannot

achieve.

This thesis explores the potential of WIVERN to significantly advance the observation of tropical cyclone dynamics. Using high-resolution simulated observations of a representative hurricane undergoing rapid intensification, this study evaluates WIVERN performance in reconstructing the 3D wind field, capturing structural asymmetries, and identifying signatures of intensification.

The specific objectives of the work are:

- To assess the ability of WIVERN to retrieve horizontal wind vectors in and around the cyclone core across multiple altitudes;
- To investigate how well the mission resolves key dynamical features such as low-level inflow, eyewall updrafts, and upper-tropospheric outflows;
- To evaluate WIVERN potential in detecting and characterizing rapid intensification events through multi-pass observations;
- To apply and validate the Holland (1980) parametric model using Doppler-derived wind profiles, quantifying changes in storm intensity over time.

By addressing these goals, the thesis contributes to the ongoing development of satellite-based strategies for monitoring extreme weather under a changing climate, offering valuable insights for future mission planning and data assimilation frameworks.

Chapter 1

Radar Remote Sensing for the Observation of TC

1.1 Introduction to Remote Sensing of the Atmosphere

Remote sensing refers to the observation of physical properties of the Earth's atmosphere, land, or oceans without direct contact. In atmospheric science, this approach allows for large-scale, continuous, and often global monitoring of dynamic phenomena such as tropical cyclones, convective systems, and jet streams. It is particularly valuable over remote or oceanic regions where in-situ observations are sparse or unavailable.

Atmospheric remote sensing can be broadly classified into two categories: passive and active systems. Passive sensors detect naturally emitted or reflected radiation, typically in the infrared or microwave spectrum. Instruments such as radiometers and infrared sounders fall into this category and are widely used to infer temperature profiles, water vapor content, and cloud-top characteristics.

Active sensors, on the other hand, transmit electromagnetic pulses and measure the energy that is backscattered by atmospheric constituents such as hydrometeors or aerosols. Examples of active systems include radar and lidar instruments. Unlike passive sensors, radar-based systems can penetrate deep cloud layers and retrieve detailed information about precipitation structure and particle motion, making them indispensable tools for weather monitoring and forecasting.

In the context of tropical cyclones, remote sensing has enabled tremendous progress in both operational forecasting and scientific understanding. Geostationary satellites provide continuous visual and infrared imagery, which is useful for tracking cyclone motion and cloud-top evolution. Polar-orbiting satellites equipped with

microwave imagers or sounders can provide insights into the internal thermodynamic and precipitation structure of storms.

Nevertheless, many of these systems offer only indirect information on wind fields or are limited by coarse spatial resolution and low revisit frequency. Scatterometers, for example, can infer surface wind vectors but may saturate in high-wind regimes, while nadir-viewing cloud radars (e.g., CloudSat, GPM) provide only narrow-swath vertical profiles. The need for direct, high-resolution observations of horizontal winds, particularly within the inner core of cyclones, remains a critical gap in the current observing system.

This gap motivates the development of novel radar missions such as WIVERN, which is specifically designed to retrieve horizontal wind vectors from precipitating clouds using Doppler measurements with a conically scanning geometry. Before introducing WIVERN in detail, the following section will present the fundamental physical principles that govern radar remote sensing in atmospheric applications.

1.2 Physical Principles of Radar Remote Sensing

1.2.1 Radar Signal Interaction with the Atmosphere

Radar remote sensing of the atmosphere is based on the transmission of short pulses of microwave radiation and the detection of the backscattered signal from atmospheric particles. The characteristics of the returned signal depend on both the properties of the radar system and the physical attributes of the scatterers, primarily hydrometeors such as cloud droplets, raindrops, snowflakes, and ice crystals (Fabry 2015).

The power received by the radar is governed by the radar equation, which, in its simplified form under Rayleigh scattering and monostatic configuration, relates the returned signal to both system parameters and the volume backscattering coefficient η. This coefficient represents the amount of power scattered back toward the radar per unit volume and depends on the number, size, phase, and dielectric properties of the hydrometeors.

A closely related but distinct quantity is the radar reflectivity factor Z, which is defined under Rayleigh assumptions as the sixth moment of the drop size distribution:

$$Z = \int_0^\infty N(D) D^6 \, dD$$

where $N(D)$ is the number concentration of hydrometeors of diameter D. The units of Z are $\mathrm{mm}^6/\mathrm{m}^3$, and it provides a wavelength-independent measure of the bulk scattering potential of a hydrometeor population, assuming spherical, liquid particles. In practice, Z is usually reported in logarithmic units as:

$$Z_{\mathrm{dBZ}} = 10 \log_{10}(Z)$$

Although Z and η are often related in meteorological applications, they are not equivalent. While Z provides a standardized metric independent of wavelength, η includes dependence on wavelength and particle dielectric properties, and directly enters the radar equation. This distinction becomes relevant when interpreting reflectivity observations at high frequencies, such as the W-band used by WIVERN.

As the radar beam propagates through the atmosphere, it experiences signal losses due to absorption and scattering by hydrometeors along its path. These losses are quantified by the extinction coefficient K_{ext}, expressed in dB/km, which combines both absorptive and scattering effects. The cumulative two-way signal loss is described by the path-integrated attenuation (PIA):

$$\mathrm{PIA}(r) = 2 \int_0^r K_{\mathrm{ext}}(s)\, ds$$

At W-band frequencies, attenuation can become severe in regions of intense precipitation, such as the eyewall of a tropical cyclone, with PIA values often exceeding 20-30 dB. This leads to underestimation of reflectivity, truncation of vertical profiles, and degradation of Doppler measurements in those regions. In practice, retrievals often include an attenuation correction step or mask out highly attenuated areas.

Another limiting factor for radar observations is the signal-to-noise ratio (SNR), defined as the ratio between the received power and the system noise floor:

$$\mathrm{SNR} = 10 \log_{10} \left(\frac{P_{\mathrm{signal}}}{P_{\mathrm{noise}}} \right)$$

When the SNR drops below a specified threshold (typically 0 or 3 dB), measurements are considered unreliable and are excluded from retrieval algorithms. Low SNR may result from weak scattering (e.g., in upper-tropospheric ice clouds), strong attenuation, or increased range. In satellite-based radar systems, SNR limitations often constrain the spatial coverage of wind and reflectivity retrievals, particularly in outer rainbands, the eye, or the upper troposphere. In addition to SNR, another important metric affecting data quality in Doppler radar observations is the signal-to-clutter ratio (SCR). This parameter quantifies the relative strength of the meteorological signal compared to undesired returns from non-meteorological sources, such as the surface or sidelobe contamination. In conically scanning radars like WIVERN, surface clutter can be particularly problematic near nadir or at low incidence angles, especially over ocean or land-water boundaries. A low SCR may lead to biased velocity estimates or false detections, particularly in regions with weak atmospheric returns. To mitigate this, a minimum SCR threshold is often imposed, typically between 3 and 10 dB, below which data are discarded or flagged

as contaminated. The use of polarization diversity and careful antenna design in WIVERN helps reduce clutter effects, but SCR remains a limiting factor in data usability near the surface or in scenes with complex backscatter characteristics.

An additional consideration is the geometry of the radar beam. The radar does not sample a point but a finite volume defined by its beamwidth and pulse length. The spatial resolution therefore degrades with increasing distance from the radar, and the power returned from the sampled volume is modulated by the antenna pattern and the pulse envelope. This volume-weighting function smooths out fine-scale gradients and can obscure small-scale structures such as inflow jets or sharp boundaries near the eyewall. At long ranges, especially from spaceborne platforms, beam broadening can introduce significant vertical and horizontal averaging, which affects the interpretability of retrieved fields.

In the context of tropical cyclone observation, these physical constraints have important implications. Strong attenuation and limited SNR reduce the effective vertical and horizontal coverage of the measurements, particularly in regions with deep convection and heavy rainfall. At the same time, beam geometry and resolution limits introduce smoothing effects that must be considered when analyzing fine-scale wind and reflectivity structures. Understanding these effects is crucial for interpreting the wind and precipitation retrievals presented in the following chapters of this thesis.

1.2.2 Doppler Radar Measurements

In addition to measuring reflectivity and attenuation, radar systems can also detect the motion of hydrometeors via the Doppler effect. When a radar transmits a pulse of electromagnetic energy and that pulse is scattered by particles moving relative to the radar, the frequency of the returned signal is slightly shifted. This frequency shift is directly related to the velocity of the particles along the radar beam, and forms the basis for Doppler radar measurements (Fabry 2015).

The Doppler effect arises from the change in phase of the backscattered signal due to the relative motion of the scatterers. In a coherent radar system, the phase of successive pulses reflected from the same scatterer is compared. If the scatterer is moving toward or away from the radar, this phase difference accumulates over time, and the rate of change of phase is proportional to the velocity along the radar line of sight. Mathematically, the measured Doppler velocity V_D is given by:

$$V_D = -\frac{\lambda}{2} \cdot \frac{d\phi}{dt}$$

where λ is the radar wavelength, and $d\phi/dt$ is the temporal derivative of the phase of the returned signal. The factor of $1/2$ accounts for the two-way propagation

of the radar pulse. The sign convention implies that motion toward the radar yields negative velocities.

Importantly, the Doppler measurement provides only the component of the wind vector projected along the radar beam, known as the radial velocity. This means that Doppler radars alone cannot observe the full three-dimensional wind field unless additional geometrical constraints or multiple beam directions are used. For ground-based radars, scanning at different azimuthal angles enables retrieval of horizontal wind vectors via volume velocity processing. Airborne Doppler systems can also take advantage of motion relative to the target or dual-beam configurations.

However, in single-beam geometries, such as vertical profiling or nadir-pointing radars, only the vertical or radial component is directly observed. This poses a limitation when interpreting storm dynamics or retrieving horizontal wind fields. Additionally, because the Doppler measurement is phase-based, there are fundamental constraints on the maximum unambiguous velocity that can be observed. This limit is determined by the radar's pulse repetition frequency (PRF) and is given by:

$$V_{\max} = \frac{\lambda \cdot \mathrm{PRF}}{4}$$

If the true radial velocity exceeds this value, aliasing occurs, and the measured velocity is wrapped within the Nyquist interval. Resolving such ambiguities requires either multiple PRFs or assumptions about wind continuity.

Another limitation is that Doppler measurements are only possible when the SNR is sufficient. In regions with low hydrometeor content or strong attenuation, such as the upper troposphere or within the eye of a tropical cyclone, the Doppler signal may be too weak to produce reliable phase estimates. Furthermore, because the observed Doppler velocity reflects the motion of the scatterers and not the air itself, it is important to assume that hydrometeors are good tracers of the wind. While this assumption generally holds in precipitating clouds, it may break down in regions with weak or variable fall speeds, especially at high altitudes.

Despite these limitations, Doppler radar remains a powerful tool for observing atmospheric motion, especially when combined with reflectivity and attenuation measurements. It provides a direct, high-resolution view of the kinematics of weather systems and forms the basis for advanced retrieval techniques used in both ground-based and satellite applications. The use of Doppler radar in spaceborne missions introduces additional challenges related to geometry and resolution, which will be discussed in the next sections when addressing observational platforms and system design.

1.3 Observational Platforms for Radar Remote Sensing

1.3.1 Airborne and Spaceborne Radar Systems: Capabilities and Limitations

Radar systems designed for atmospheric observation can be deployed from both airborne and spaceborne platforms, each offering unique strengths and facing specific limitations in terms of spatial resolution, temporal sampling, coverage, and instrument sensitivity. These systems have become essential tools in the study of TCs, enabling the monitoring of wind fields, precipitation structures, and convective organization in regions that are otherwise difficult to access.

Airborne radar systems, such as those onboard research aircraft operated by NOAA and NASA, have long provided high-resolution measurements of TC inner-core structure. Tail Doppler radars (TDRs), for example, scan conically around the aircraft flight path and retrieve three-dimensional wind fields at horizontal resolutions of 1–2 km. These radars are capable of capturing key features such as low-level inflow, eyewall convection, vortex tilt, and upper-level outflow. Their flexibility in targeting specific storm regions allows adaptive sampling strategies, making them extremely valuable for operational forecasting and model initialization. However, airborne campaigns are logistically complex, costly, and limited to certain geographic areas and time windows, primarily the North Atlantic hurricane basin during field experiments. As noted by Fabry (2015), while airborne Doppler radars can achieve high spatial and temporal resolution, their episodic and regional coverage limits their contribution to global cyclone climatology.

Spaceborne radar systems offer the advantage of regular, near-global sampling and consistent instrument calibration (A. Battaglia, Kollias, et al. 2020). Several missions have demonstrated the value of spaceborne radar in observing precipitation and cloud structure. The Tropical Rainfall Measuring Mission (TRMM) and its successor, the Global Precipitation Measurement (GPM) Core Observatory, both featured precipitation radars operating at Ku- and Ka-band frequencies, providing vertical profiles of rain rate and convective depth across the tropics. Similarly, CloudSat, equipped with a nadir-pointing W-band radar, revolutionized our understanding of cloud microphysics and vertical structure, particularly in non-precipitating regions. However, due to its narrow swath and single-beam geometry, CloudSat was not designed for wind retrieval, and did not include Doppler capability.

Efforts to retrieve wind from spaceborne radar systems have faced significant technical challenges. One limitation is geometric: nadir-viewing radars are sensitive primarily to vertical motion, and cannot resolve horizontal winds without additional viewing angles. Furthermore, obtaining meaningful Doppler shifts requires high

phase sensitivity and sufficient signal-to-noise ratio, which can be difficult to achieve from orbit, especially in attenuating media like rain or ice clouds.

Some progress has been made using active optical systems. The Aeolus mission, launched by ESA in 2018, demonstrated the feasibility of global wind retrieval using a Doppler lidar. While Aeolus provided valuable wind profiles in clear air, lidar technology suffers from strong attenuation in cloudy and precipitating regions, severely limiting its usefulness in tropical cyclone environments. This observational gap is consistently highlighted in the literature, including in Ricciardulli et al. (2023), where the lack of direct wind measurements in TCs is identified as a critical weakness in the current global observing system.

Emerging missions, such as EarthCARE, aim to address some of these limitations by combining cloud radar and lidar with additional radiometric instruments. However, they still lack the ability to resolve horizontal winds in precipitating regions at scales relevant to cyclone dynamics. Moreover, the fixed nadir viewing geometry limits their ability to observe rotational structures or asymmetric flow patterns typical of TCs.

Overall, while existing airborne and satellite platforms have significantly advanced our understanding of tropical cyclone structure and precipitation, none currently offer the combination of resolution, coverage, and Doppler capability required to directly observe horizontal wind fields within the core of precipitating systems. The need for all-weather, high-resolution, wide-swath wind observations from space remains unmet and motivates the development of next-generation Doppler radar missions specifically tailored for storm-scale dynamics.

1.4 The WIVERN Mission: Objectives and Technological Innovations

WIVERN (WInd VElocity Radar Nephoscope) is a cutting-edge candidate mission proposed under ESA's Earth Explorer 11 program. Its innovative design addresses a long-standing gap in global atmospheric observation by enabling the first-ever routine retrieval of horizontal wind profiles within cloudy and precipitating regions (Illingworth et al. 2018; A. Battaglia, Martire, et al. 2022; Tridon et al. 2023; A. Battaglia, Rizik, et al. 2025; ESA 2025). Unlike previous satellite platforms, such as Aeolus (lidar-clear-air only) or CloudSat and GPM (hydrometeor profiling without Doppler), WIVERN uniquely combines in-cloud Doppler radar with wide swath coverage and high spatial resolution. The instrument architecture centers around a dual-polarized W-band (94 GHz) Doppler radar mounted on a satellite in sun-synchronous orbit (500 km altitude), executing a conical scan at approximately 12 rpm. The instrument observes each atmospheric column with an incidence angle of 42° off-nadir, enabling measurements of the horizontal line-of-sight (HLOS) wind

(Illingworth et al. 2018; A. Battaglia, Martire, et al. 2022). In the majority of the swath multiple looks are available. These dual-angle HLOS measurements allow reconstruction of full horizontal wind vectors when processed through geometric inversion algorithms (Alessandro Battaglia et al. 2024; Silva et al. 2025). A schematic illustration of the WIVERN scanning concept is shown in Figure 1.1, where the swath intersects a tropical cyclone. The Level-1 radar reflectivity product is shown across the conical scan, while the underlying total hydrometeor content is visualized in the outer part of the storm with a blue color scale (white indicating high content). This highlights WIVERN ability to resolve both microphysical and dynamical features across a wide area.

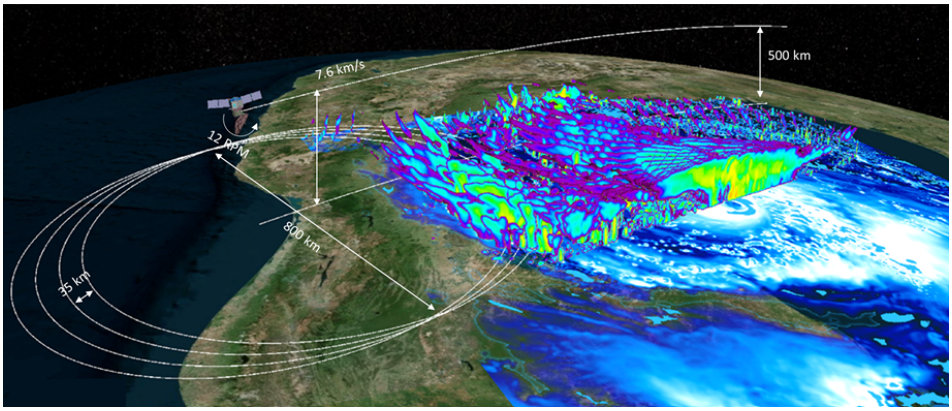

Figure 1.1: Conceptual representation of WIVERN conical scanning strategy as it observes a tropical cyclone. The swath crosses the eye of the storm, with the radar reflectivity (Level-1 product) displayed across the scan. On the eastern edge of the cyclone, outside the radar coverage, the total hydrometeor content is shown using a blue color scale (light shades indicating higher concentrations). Note: the geometric proportions are illustrative and not to scale. Source: A. Battaglia, Recupero, et al. (2025).

1.4.1 Key Technological Innovations

The WIVERN mission introduces a set of technological solutions specifically tailored to meet the stringent requirements of Doppler wind observations from space. These innovations address challenges related to signal attenuation, retrieval accuracy, temporal and spatial coverage, and calibration (A. Battaglia, Martire, et al. 2022). The most significant features of the mission architecture and design are summarized below:

1. **Deployable 2.5–3 m Antenna.** A large antenna aperture is required to achieve the gain necessary for Doppler velocity measurements with an RMS

error below 2 m/s. This configuration ensures a footprint resolution of approximately 6 km (horizontal) by 500 m (vertical), which is well-suited for observing mesoscale dynamics.

2. **Polarization Diversity and Radiometric Mode.** Dual-polarization channels allow for extending Doppler Nyquist interval up to 40 m/s (i.e. hurricane-force winds), practically resolving the Doppler dilemma (A. Battaglia, Tanelli, et al. 2013; Wolde et al. 2019). The instrument also includes a radiometric mode to measure brightness temperature (A. Battaglia and Panegrossi 2020).

3. **Wide Swath and Revisit Frequency via Conical Scanning.** The conical scanning strategy provides a swath of approximately 800 km, supporting near-daily revisit capabilities poleward of 50° latitude (Tridon et al. 2023). In tropical regions, the revisit interval is slightly longer but still allows for frequent coverage of rapidly evolving systems.

4. **Onboard Calibration and Mispointing Correction.** Detailed simulations account for mispointing errors, including azimuth and elevation offsets, which are correctable in orbit through calibration strategies using surface returns and cloud echoes (Scarsi et al. 2023). Typical biases remain below 0.3-0.6 m/s.

5. **Comprehensive End-to-End Simulator.** The mission development includes a sophisticated end-to-end simulator that models the full signal acquisition chain, incorporating beam geometry, mispointing effects (e.g. thermal distortions, platform vibrations, see Manconi et al. 2025), surface clutter, attenuation, and Doppler aliasing (A. Battaglia, Dhillon, et al. 2018; A. Battaglia, Martire, et al. 2022; A. Battaglia, Rizik, et al. 2025). Simulated retrievals confirm Doppler errors below 2 m/s in sufficiently reflective cloud volumes ($Z > -20$ dBZ).

6. **Robust Performance Under Realistic Conditions.** Extensive testing under conditions with wind shear, non uniform beam filling (A. Battaglia, Recupero, et al. 2025), and ground clutter (Coppola et al. 2025) demonstrates that the instrument can maintain performance within the mission requirements. The primary limitations arise in regions with very low reflectivity, strong vertical shear, or near-surface clutter.

7. **Novel Cross-Calibration Approach.** Due to its conical scan geometry, WIVERN cannot rely on nadir-looking ocean surfaces for calibration. Instead, gain calibration is performed using statistical comparisons with known cloud reflectivity distributions, co-registered with other satellite missions such as GPM and EarthCARE. These methods achieve gain calibration stability better than 1 dB over weekly timescale (A. Battaglia, Scarsi, et al. 2023).

1.4.2 Scientific Goals and Relevance to Tropical Cyclone Observation

WIVERN is designed to address several pressing scientific and operational needs in atmospheric science, particularly those related to cloud-resolving wind observations. One of its primary goals is the retrieval of HLOS wind vectors within clouds and precipitation, at spatial scales greater than 20 km, with an accuracy suitable for data assimilation in numerical weather prediction (NWP) models (Sasso et al. n.d.). This capability is particularly valuable for TC environments, where in-cloud wind fields remain largely unobserved due to instrumental and geometric limitations of existing systems (Illingworth et al. 2018; A. Battaglia, Martire, et al. 2022; Tridon et al. 2023).

By providing all-weather Doppler wind measurements across an 800 km swath, WIVERN enables the global monitoring of dynamical processes that drive storm evolution. In precipitating systems such as TCs, the radar's ability to penetrate clouds and retrieve wind profiles allows for the detailed characterization of key features including low-level inflow, mid-level convergence, and upper-level outflow. These elements play a fundamental role in vortex intensification, eyewall replacement cycles, and RI. Furthermore, WIVERN offers unique advantages for TC lifecycle analysis. Its sun-synchronous orbit and conical scan geometry ensure quasi-global coverage and revisit capabilities, allowing it to observe storms at multiple developmental stages, from genesis to decay. This temporal continuity supports the detection of structural changes in the wind field, which often precede rapid changes in intensity.

Further insight into WIVERN capability to monitor tropical cyclones comes from an analysis presented in A. Battaglia, Recupero, et al. (2025), where both the historical distribution of intense TCs and the revisit potential of the WIVERN mission were evaluated. Figure 1.2 summarizes these findings. Panel (a) displays the ground-tracks of all tropical cyclones recorded globally over the past 35 years that reached at least Category 1 intensity (maximum wind speed > 33 m/s), based on IBTrACS data. Track colors encode the maximum intensity reached by each storm: from blue (tropical storm) to violet (Category 5). This visualization highlights the wide geographical extent of TC activity, emphasizing the importance of satellite-based platforms with broad coverage. Panel (b) evaluates WIVERN revisit statistics relative to the storm center. The boxplots show the distribution of revisit intervals (in days) for passes within different radial distances ($D = 50$, 100, and 200 km) from the TC eye. For each radius, the median, interquartile range, and outliers are plotted. The percentages annotated above the boxes represent the probability of missing the storm entirely at that distance. For instance, at a 200 km threshold, the chance of missing a TC drops below 10%, illustrating WIVERN capacity to frequently sample the storm core. This revisit performance

is particularly valuable for capturing critical phases in cyclone evolution, such as RI, which often occur on timescales of less than 24 hours. Thanks to its scanning geometry and sun-synchronous orbit, WIVERN can provide at least two passes within 12 to 24 hours over the same TC, enabling monitoring before and after key structural transitions. This sampling frequency, combined with the Doppler capability, positions WIVERN as a highly relevant instrument for operational monitoring and scientific study of TCs.

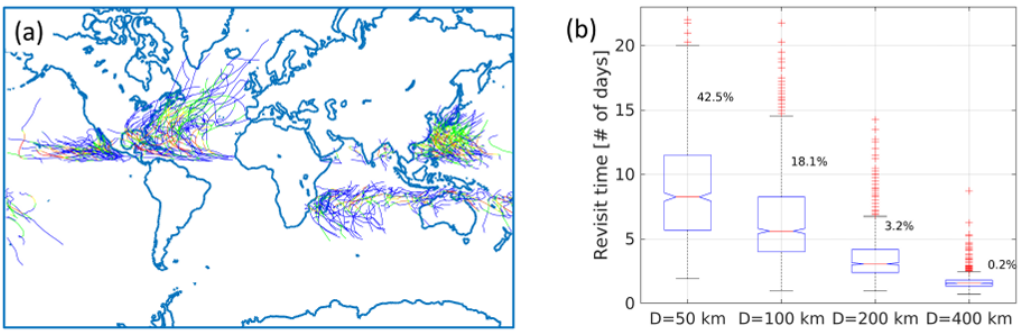

Figure 1.2: (a) Historical tracks of tropical cyclones reaching at least Category 1 intensity in the past 35 years, color-coded by Saffir–Simpson category. (b) WIVERN revisit time statistics showing the distribution of days between consecutive passes within 50, 100, and 200 km from the TC center. Percentages indicate the probability of entirely missing the TC at each distance threshold. Source: A. Battaglia, Recupero, et al. (2025).

Unlike traditional passive sensors, which infer motion indirectly from temperature or cloud motion tracking, WIVERN measures the Doppler shift of hydrometeor returns, providing direct estimates of wind even in heavily precipitating and optically thick regions. The use of a dual-beam configuration at 35° off-nadir allows for full horizontal wind vector retrievals through geometric inversion, further enhancing the utility of the data for dynamical analysis. In addition to wind vectors, WIVERN will generate vertical profiles of radar reflectivity, hydrometeor phase, and path-integrated attenuation, as well as brightness temperature fields through its radiometric channel. These products extend the legacy of CloudSat by 40× in spatial coverage and add critical velocity information to improve the physical understanding of storm dynamics and cloud processes. Simulated data assimilation experiments suggest that incorporating WIVERN-style Doppler wind observations into tropical cyclone forecast models could reduce root-mean-square (RMS) errors in u- and v-wind components by 5–10%, demonstrating the mission's strong potential impact on operational forecasting and early warning systems. From a technical perspective, Phase-0 feasibility studies confirm that the WIVERN

concept meets ESA Earth Explorer mission requirements. End-to-end simulations show that HLOS wind accuracy remains below 2 m/s within most cloudy regions, and that retrieval performance is robust against sources of error such as beam mispointing, clutter contamination, and cross-polarization leakage (A. Battaglia, Martire, et al. 2022; Tridon et al. 2023).

In summary, WIVERN represents a transformational advance in satellite remote sensing, delivering the capability to directly observe winds within the most dynamic and meteorologically important regions of the atmosphere. Its unique capacity to capture high-resolution, multi-layered wind structures in tropical cyclones makes it exceptionally well-suited for addressing the scientific questions posed in this thesis, particularly regarding the monitoring and prediction of rapid intensification events.

Chapter 2

Hurricane Dynamics

2.1 General Structure of a Tropical Cyclone

Tropical cyclones are intense, warm-core low-pressure systems that form over warm ocean waters in the tropics and subtropics. Driven by the release of latent heat from deep convection, they represent one of the most powerful and organized phenomena in the atmosphere (Houze 2010). Depending on geographic location, these storms are referred to as *hurricanes* (Atlantic and Eastern Pacific), *typhoons* (Western Pacific), or simply *cyclones* (Indian Ocean and Southern Hemisphere). Figures 2.1-2.2 show Hurricane Florence from the ISS, as captured by astronaut Alexander Gerst (Pappas 2018).

2.1.1 Synoptic-Scale Organization

At the macroscale, a mature TC typically displays a nearly axisymmetric structure composed of:

- A central, often cloud-free eye, typically 20-60 km in diameter;
- A surrounding ring of intense convection known as the eyewall;
- Outer spiral rainbands that wrap cyclonically around the center, interspersed with regions of subsidence and stratiform precipitation.

Vertically, TCs span the entire tropical troposphere (16-18 km in height) and are commonly divided into three dynamical layers:

- **Boundary layer (0-2 km):** Characterized by frictionally driven radial inflow, turbulent mixing, and surface fluxes of heat and moisture.
- **Mid-troposphere (2-8 km):** Dominated by deep convection and strong ascent in the eyewall, accompanied by stratiform precipitation.

- **Upper troposphere (8-16 km):** Marked by divergent outflow aloft, which ventilates the storm and supports its convective core.

Figure 2.1: Hurricane Florence viewed from the International Space Station by astronaut Alexander Gerst on 12 September 2018. Source: Pappas 2018.

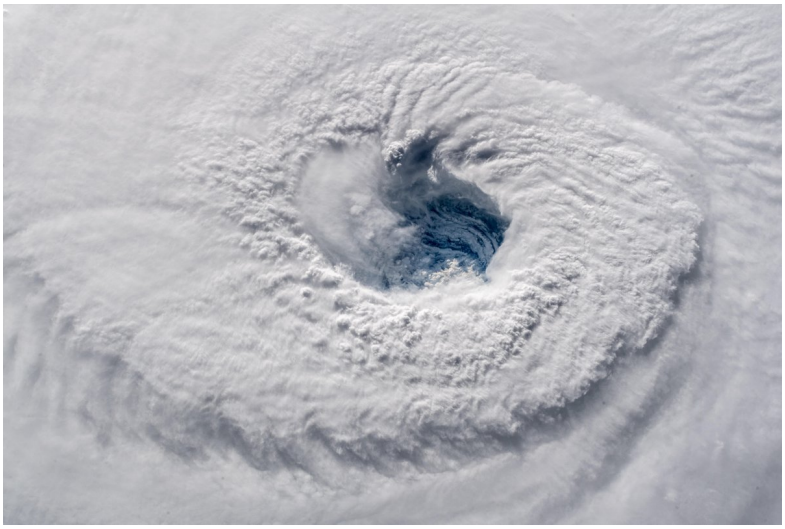

Figure 2.2: Zoom over the eye of Hurricane Florence. Source: Pappas 2018.

2.1.2 Internal Regions: Eye, Eyewall, Inflow, and Outflow

The internal structure of a TC is governed by dynamically distinct but interconnected regions:

Eye. The eye is a calm, warm region at the storm center, typically 20-60 km across, characterized by light winds, subsidence, and often clear skies. It forms as a result of mass conservation, with descending motion replacing the rapidly rising air of the surrounding eyewall. This descent produces adiabatic warming, reinforcing the warm-core structure aloft. Despite its apparent tranquility, the eye can host small-scale turbulence and mesovortices, particularly in stronger storms.

Eyewall. Encircling the eye, the eyewall is the region of strongest winds and heaviest rainfall. It consists of deeply convective clouds where low-level air spirals inward and is forced upward, releasing latent heat that fuels the storm's energy cycle. The eyewall defines the radius of maximum wind (RMW) and is the principal driver of the warm-core anomaly through intense diabatic heating.

Inflow Layer. This region extends from the surface to approximately 2 km altitude and is where frictional convergence drives air inward toward the cyclone center. The inflow layer transports heat and moisture from the ocean surface into the eyewall and rainbands, serving as the primary energy source for deep convection.

Outflow Layer. Situated in the upper troposphere (typically 12-16 km), the outflow region disperses mass from the convective core through diverging winds aloft. Well-channeled and symmetric outflow supports storm intensification by lowering static stability and enabling persistent vertical motion. Outflow can be influenced by upper-level troughs or jets, and disruptions in this layer often limit intensification.

2.1.3 Warm-Core Structure and Circulation

A defining dynamical trait of TCs is their warm-core structure: latent heating from condensation within the eyewall generates a vertical column of anomalously warm air, especially in the mid-to-upper troposphere. This warm anomaly leads to hydrostatic pressure falls at the surface, reinforcing the radial pressure gradient and strengthening the low-level winds in a positive feedback loop.

TC circulation consists of:

- **Primary circulation:** Cyclonic tangential winds that peak near the RMW and decrease radially outward.

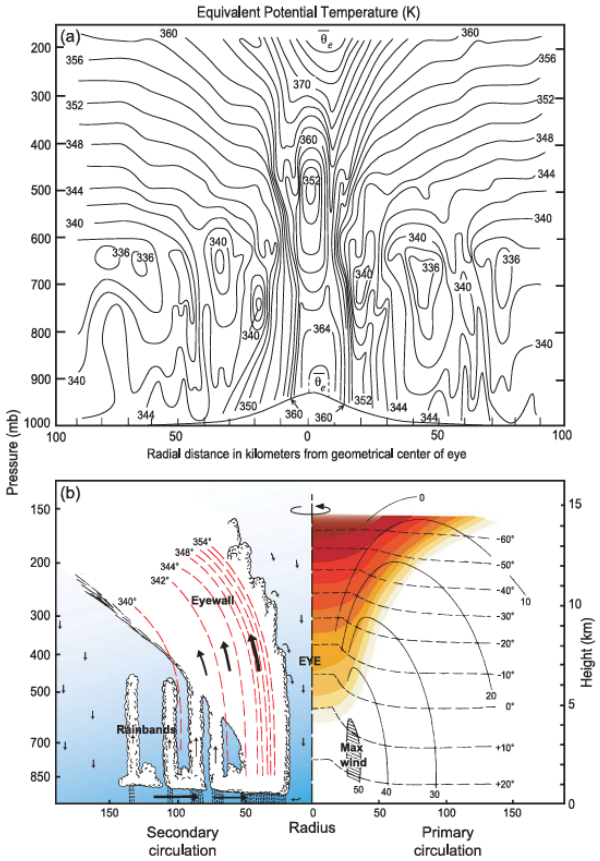

Figure 2.3: Schematic representation of the thermodynamic and dynamic structure of a tropical cyclone. **(a)** Contours of equivalent potential temperature (θ_e) across the storm core illustrate the warm core anomaly in the eye and upper troposphere. **(b)** Conceptual depiction of secondary circulation (left) and primary tangential wind field (right). Rainbands, the eyewall, and the distribution of upward and downward motion are indicated. Source: Houze (2010).

- **Secondary circulation:** A thermally driven overturning flow composed of radial inflow, upward motion, and upper-level outflow, as presented in Figure 2.3. This component governs energy and momentum transport and is closely tied to storm evolution.

2.1.4 Intensity Classification: The Saffir–Simpson Scale

Operational classification of tropical cyclones is based on sustained surface wind speeds, using the Saffir–Simpson Hurricane Wind Scale (SSHWS). This categorization, shown in Table 2.1, is central to hazard communication and preparedness

strategies (National Hurricane Center 2023).

Table 2.1: Saffir–Simpson Hurricane Wind Scale. Source: National Hurricane Center (2023).

Category	Description	Wind Speed (1-min sustained)
1	Minimal hurricane	119–153 km/h (74–95 mph)
2	Moderate hurricane	154–177 km/h (96–110 mph)
3	Major hurricane	178–208 km/h (111–129 mph)
4	Severe hurricane	209–251 km/h (130–156 mph)
5	Catastrophic hurricane	$\geq$252 km/h ($\geq$157 mph)

2.1.5 Secondary Structural Features

Many mature cyclones exhibit structural features beyond the canonical eye and eyewall, particularly during phases of reorganization or interaction with the environment.

Eyewall Replacement Cycles and Moats. In intense storms, a secondary eyewall may form and contract inward, replacing the original eyewall in a process known as an eyewall replacement cycle (ERC). The region between the inner and outer eyewalls, known as the moat, typically shows reduced convection and weaker winds. ERCs can temporarily weaken storms, but often lead to increased storm size and renewed intensification.

Wind Asymmetries. Asymmetric wind fields are common, especially in sheared environments or near land. Wind maxima and deep convection are often displaced downshear or offset from the center, altering precipitation patterns and storm impacts. These asymmetries are particularly important for forecasting landfall hazards and rainfall distributions.

Convective Bursts. Sudden, localized regions of intense convection, convective bursts, are frequently observed in or near the eyewall and are closely linked to rapid intensification. These bursts enhance latent heat release and may locally strengthen the warm core, increase updraft strength, and promote upper-level divergence. Monitoring such features is essential for short-term intensity forecasts.

2.2 Formation and Intensification Mechanisms

The formation of a tropical cyclone, or cyclogenesis, occurs when a preexisting disturbance in the tropical atmosphere becomes sufficiently organized to sustain a closed surface circulation and a coherent warm core. While many tropical waves or convective clusters form in the tropics, only a small fraction develop into tropical cyclones, highlighting the importance of favorable environmental conditions and internal organization (Houze 2010).

Several key environmental factors must align for genesis to occur:

- **Warm sea surface temperatures** (typically above 26.5°C), which provide the energy source for deep convection through evaporation and latent heat release.
- **Sufficient Coriolis force**, which ensures that the convective system can develop rotation; this typically requires formation at least 5° away from the equator.
- **High humidity in the lower to mid-troposphere**, which supports sustained convection and limits the erosion of updrafts by dry air entrainment.
- **Weak to moderate vertical wind shear**, allowing convective towers and vorticity to remain vertically aligned.
- **A preexisting low-level disturbance**, such as an easterly wave or an area of enhanced vorticity, which can act as a seed for cyclonic organization.

Cyclogenesis involves the gradual concentration of vorticity and thermodynamic organization, often mediated by convective systems. According to Houze (2010), mesoscale convective systems (MCSs) play a central role by creating stratiform regions and mesoscale convective vortices (MCVs) that consolidate rotation. In addition, vertically aligned, deep convective bursts, known as vortical hot towers (VHTs), are crucial to the spin-up process. These towers generate intense updrafts that locally stretch vorticity and release large amounts of latent heat, contributing to the formation of a mid-level warm core. Once a tropical depression forms, further intensification is driven by a positive thermodynamic feedback: surface winds increase, enhancing oceanic heat and moisture fluxes; this, in turn, fuels more intense convection and latent heating, further deepening the cyclone's central pressure.

Rapid intensification (RI) is a distinct phase in which the maximum sustained winds increase by at least 30 kt (15.4 m/s) in 24 hours. RI typically occurs when convective activity becomes symmetric and closely aligned with the storm's center of circulation. The establishment of a mature eyewall, with persistent updrafts and

continuous latent heat release, is essential to sustaining RI. Environmental factors such as vertical wind shear and dry air intrusion can inhibit or delay intensification. However, as noted by Houze (2010), some tropical cyclones may undergo RI even in moderately sheared environments, provided that inner-core convective structures, especially VHTs and convective bursts, remain coherent and concentrated near the storm center. In addition to favorable large-scale conditions, such as low shear, high sea surface temperatures, and moist mid-levels, RI is often driven by internal processes occurring at the mesoscale. In particular, convective bursts, consisting of short-lived intense updrafts near the RMW, have been observed to play a crucial role. These features can locally enhance the warm-core anomaly and accelerate low-level inflow through pressure falls, triggering a feedback loop that promotes intensification. A striking example is provided by Hurricane Patricia (2015), which underwent one of the most extreme cases of RI ever recorded (Fox and Judt 2018). Within a 24-hour period, Patricia's sustained winds increased by over 100 kt, tripling the minimum threshold for RI. This extraordinary development occurred over exceptionally warm waters (>30.5°C) and low-shear conditions (<4 m/s), but was also linked to Patricia's compact inner-core structure and persistent convective symmetry. Observations and modeling studies (Rogers, Aberson, et al. 2017) indicate that Patricia's intensification was closely associated with organized eyewall convection and efficient ventilation aloft via a robust upper-level outflow channel. The timeline and magnitude of this rapid wind increase are illustrated in Figure 2.4, which compiles estimates from multiple observation sources (Kimberlain et al. 2016).

The rapid contraction of the RMW, enhancement of updraft strength, and acceleration of tangential winds suggest that RI is not simply an intensification of usual processes, but a nonlinear transition involving changes in the internal energy distribution of the storm. This poses considerable challenges for operational forecasting, as small-scale fluctuations in convection or outflow may trigger major intensity shifts. Understanding the coupling between inner-core dynamics and environmental factors is thus essential to predicting RI. From an observational perspective, the ability to retrieve horizontal wind vectors across the storm, particularly in and around the eyewall, offers critical insight into the mechanisms that govern rapid changes in intensity. This is one of the key motivations behind the WIVERN mission, which aims to observe such structures with unprecedented spatial and temporal resolution.

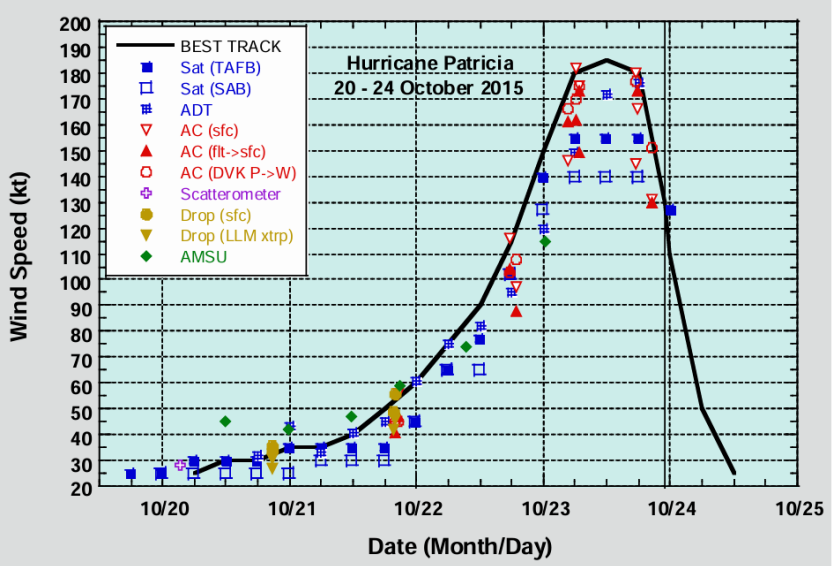

Figure 2.4: Time series of wind speed estimates for Hurricane Patricia (20–24 October 2015), from multiple observation platforms including satellite estimates (TAFB, SAB, ADT), aircraft reconnaissance (surface and extrapolated), scatterometer, and dropwindsondes. The black line indicates the best track maximum sustained winds. The figure illustrates the exceptional rapid intensification of Patricia, reaching peak sustained winds of 185 kt in less than 48 hours. Source: Kimberlain et al. 2016.

Chapter 3

Methodology

3.1 Overview of the Methodology

The methodology adopted in this study is grounded in the simulation of WIVERN Doppler radar observations and their application to the retrieval of horizontal wind fields within TCs. Rather than relying on real mission data, still unavailable at this development stage, the analysis is based on a detailed end-to-end simulator capable of replicating the performance of the WIVERN system under realistic meteorological and instrumental conditions, as described by A. Battaglia, Recupero, et al. (2025).

The overall approach can be summarized in three main phases:

1. Generation of realistic wind and reflectivity fields from a high-resolution numerical weather prediction (NWP) model simulating a tropical cyclone.

2. Simulation of WIVERN Doppler measurements based on the radar scanning geometry and sensor specifications, including effects of attenuation and viewing angle.

3. Application of a retrieval algorithm to invert the Doppler observations and reconstruct the horizontal wind field, with specific attention to spatial constraints and sampling geometry.

This framework enables a detailed evaluation of WIVERN performance in capturing the dynamic structure of intense TCs, particularly during phases of rapid intensification.

3.2 Atmospheric Model and TC Simulation

The tropical cyclone analyzed in this study, named Hurricane Milton, was synthetically generated using version 4.6.1 of the Weather Research and Forecasting (WRF) model (Powers et al. 2017; Skamarock et al. 2019). The simulation was designed to serve as the meteorological reference scenario for assessing WIVERN wind retrieval performance. WRF was configured in a two-way nested domain structure, with the innermost moving nest operating at 1.5 km horizontal resolution and ∼500 m vertical grid spacing, allowing explicit resolution of key mesoscale structures such as eyewall convection, spiral rainbands, and boundary-layer inflow. The model was initialized with ERA5 reanalysis on 5 October 2024 and integrated forward for 6 days, using updated lateral boundary conditions every 6 hours. Physics parameterizations were optimized for tropical cyclone intensification: the Thompson aerosol-aware microphysics scheme, RRTMG radiation, RUC land surface model, and YSU planetary boundary layer scheme were employed. No cumulus parameterization was used in the innermost domain. To reduce excessive numerical diffusion, known to suppress cyclone growth, turbulence closure coefficients (Smagorinsky and TKE) were reduced to 12.5% of their default values. Ideal environmental conditions were prescribed: low vertical wind shear, high sea surface temperatures ($> 30.5°$C), and elevated tropospheric humidity. Under these conditions, Hurricane Milton underwent RI, evolving from a weak tropical storm to a Category 4 hurricane within approximately 72 hours (see Figure 3.1).

The modeled storm closely followed a realistic path consistent with WIVERN expected observational geometry, providing a physically meaningful scenario for simulating satellite-based Doppler retrievals.

3.3 Simulated WIVERN Observations

To simulate WIVERN measurements, the hourly three-dimensional output fields from the WRF model were ingested into the ESA-developed end-to-end simulator created during the Phase-0 activities of the Earth Explorer 11 program (A. Battaglia, Martire, et al. 2022). These fields include horizontal and vertical wind components, temperature, pressure, total hydrometeor content, and radar reflectivity. The simulator reproduces WIVERN conically scanning W-band Doppler radar geometry, orbital propagation, and antenna rotation. At each radar beam location, the Doppler line-of-sight (LOS) velocity is computed by projecting the local wind vector onto the radar beam, subtracting satellite motion and hydrometeor fall speed. Instrumental and atmospheric effects are explicitly modeled:

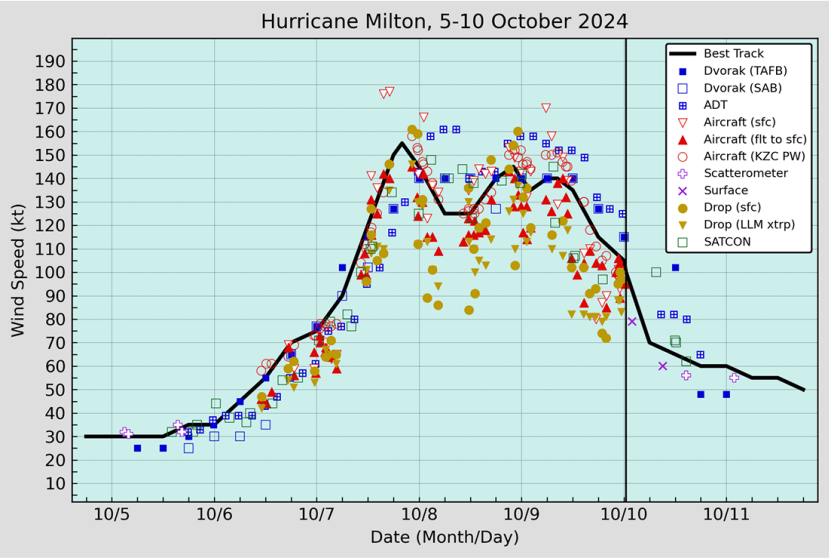

Figure 3.1: Time series of wind speed estimates for Hurricane Milton (5–10 October 2024) from multiple observing systems. The thick black line shows the best track intensity. Note the period of rapid intensification between 6 and 7 October. Source: Beven II et al. (2025).

- **Attenuation:** PIA is computed using extinction coefficients along the radar path;
- **Thermal noise:** random noise is added according to expected SNR;
- **Quality filtering:** observations are retained only if reflectivity exceeds -18 dBZ and vertical wind speed is below 2 m/s.

Simulated overpasses cover 39 WRF snapshots between 6 October at 10:00 UTC and 8 October at 00:00 UTC. Each pass lasts 200 seconds and includes 40 full antenna rotations, with both forward- and backward-looking views. Only tracks passing within 400 km of the TC center are retained to ensure valid observation geometry.

This simulation framework yields synthetic Doppler velocity measurements consistent with the expected WIVERN Level-1B product. These data serve as direct input for the horizontal wind retrieval algorithm presented in Section 3.4, enabling quantitative evaluation of WIVERN ability to reconstruct wind fields during rapid intensification and varying shear regimes.

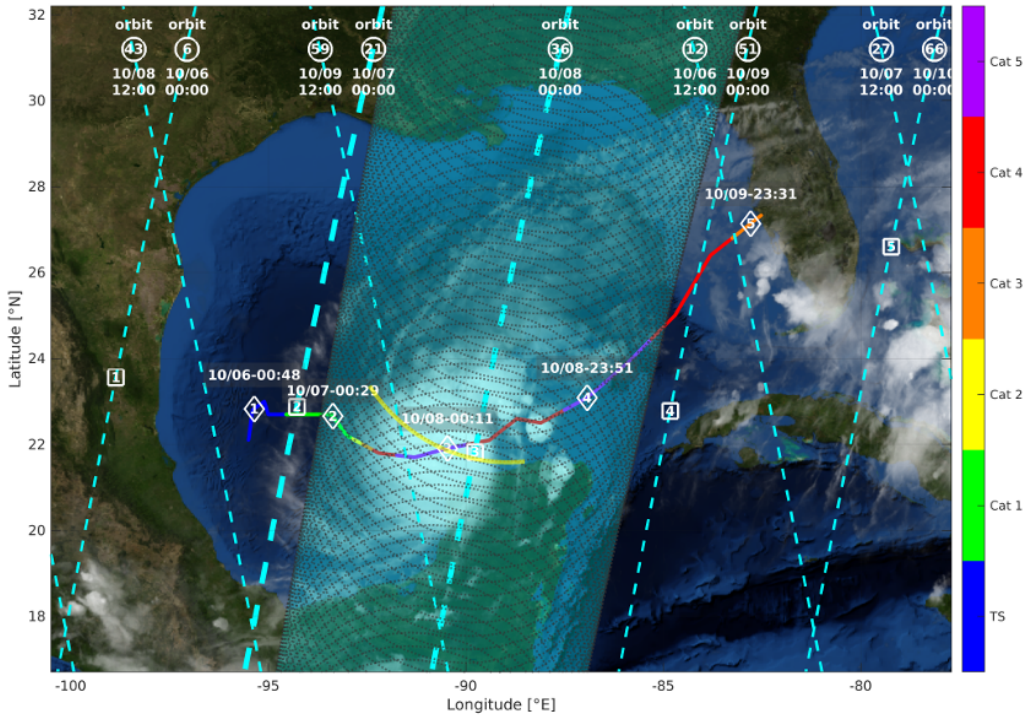

Figure 3.2: Trajectory of Hurricane Milton from 06 to 10 October 2024, overlaid with WIVERN satellite ground tracks (cyan dashed lines). Color-coded markers indicate the hurricane intensity (according to the Saffir–Simpson scale), while diamonds and squares denote the position of the TC eye and the satellite closest approach, respectively. The scanning pattern of WIVERN is illustrated for the descending orbit on 08 October. Source: A. Battaglia, Recupero, et al. (2025)

3.4 Measurement Geometry and Sampling Strategy

The reconstruction of horizontal wind fields from WIVERN observations relies critically on the geometry of measurement and the spatial sampling strategy (Silva et al. 2025). Rather than measuring winds directly, the radar captures Doppler shifts resulting from the projection of atmospheric motion along the LOS of each beam. The conical scan pattern of WIVERN, combined with its forward- and backward-looking dual-beam configuration, enables multiple azimuthal views of the same atmospheric volume, an essential feature for wind vector inversion.

As shown in Figure 3.3, each Doppler velocity V_{LoS} is related to the three-dimensional wind vector $\vec{V} = (u, v, w)$ through:

$$V_{\mathrm{LoS}} = \alpha' u + \beta' v + \gamma' w,$$

where the coefficients α', β', and γ' depend on the radar beam geometry:

$$\alpha' = \sin(\theta_I)\sin(\psi - \psi_N), \quad \beta' = \sin(\theta_I)\cos(\psi - \psi_N), \quad \gamma' = \cos(\theta_I),$$

with θ_I denoting the fixed incidence angle, ψ the beam azimuth, and ψ_N the satellite ground-track azimuth.

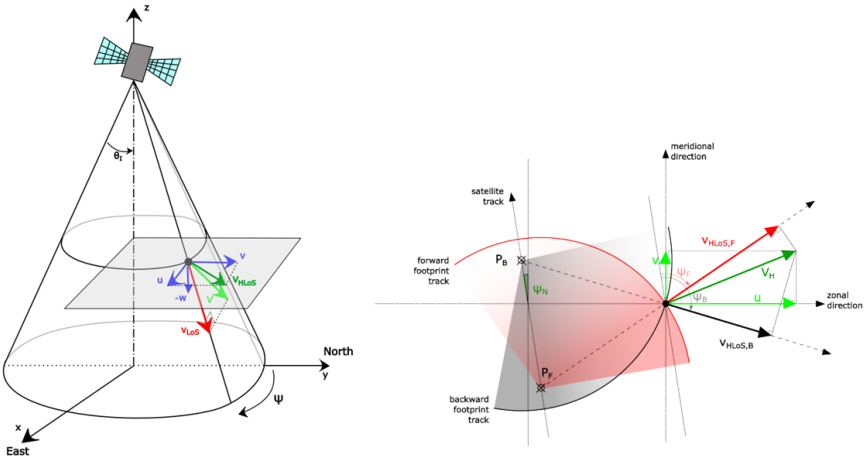

Figure 3.3: Schematic representation of the WIVERN Doppler geometry. (Left) The conical scanning geometry defines the incidence angle θ_I, and the Doppler measurement V_{LoS} is a projection of the 3D wind vector. (Right) Geometry of forward and backward views in the horizontal plane. The horizontal LoS velocities $V_{\mathrm{HLoS,F}}$ and $V_{\mathrm{HLoS,B}}$ are projections of the horizontal wind vector (u, v) along two different azimuths. Source: Silva et al. (2025).

In regions outside deep convection, the vertical wind speed w is often negligible, allowing simplification to the HLOS velocity:

$$V_{\mathrm{HLoS}} = \alpha u + \beta v, \quad \text{with } \alpha = \frac{\alpha'}{\sin(\theta_I)}, \quad \beta = \frac{\beta'}{\sin(\theta_I)}.$$

The diversity of azimuthal viewing angles is not uniform across the swath. Figure 3.4 illustrates how beams overlap more densely near the swath edges, resulting in enhanced angular sampling. Conversely, central regions may suffer from limited directional diversity, degrading the retrieval performance unless supported by stronger regularization.

Each valid HLOS measurement provides a linear constraint on the local horizontal wind vector. These constraints are combined using a weighted least-squares

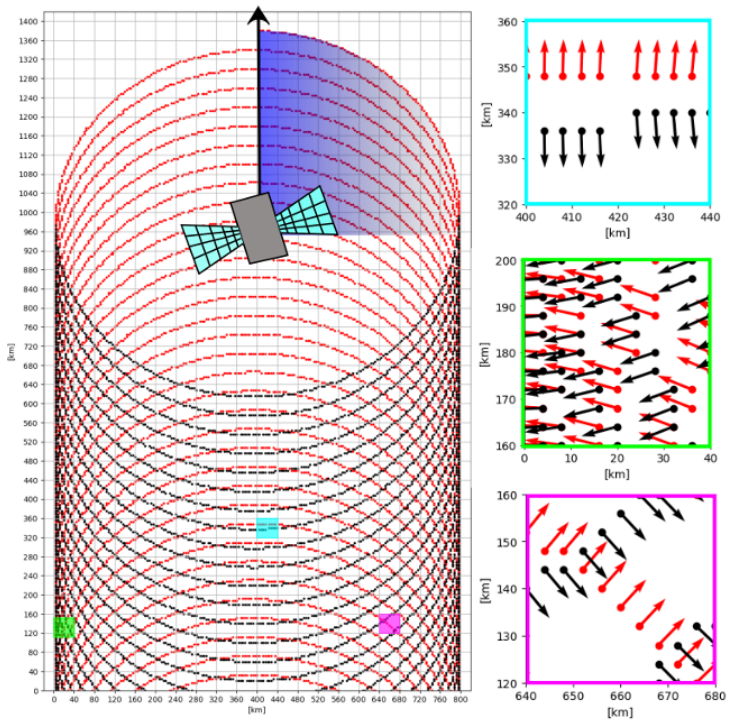

Figure 3.4: WIVERN sampling geometry. Red and black dots represent forward- and backward-looking beams, respectively. Three insets on the right show measurement geometry within selected $40\times40\,\mathrm{km}^2$ boxes: green and magenta (edges of the swath) display rich azimuthal sampling, while the cyan (center) is more limited. Source: Silva et al. (2025)

approach, where nearby observations contribute more to the estimate at a given grid point l. The spatial weighting is controlled by a Gaussian kernel:

$$\xi_i^{(l)} = \exp\left[-\left(\frac{r_i^{(l)}}{L}\right)^2\right],$$

with $r_i^{(l)}$ denoting the distance between the observation and the grid node, and L the correlation length.

Figure 3.5 shows the spatial relation between measurement points (green dots) and retrieval grid nodes (red triangles). In areas where directional constraints are insufficient—e.g., near the swath center or in regions of low reflectivity—additional physical assumptions are introduced to stabilize the inversion. Chief among them is the assumption of horizontal mass conservation under the anelastic approximation:

$$\nabla \cdot \vec{u} = \frac{\partial u}{\partial x} + \frac{\partial v}{\partial y} = 0.$$

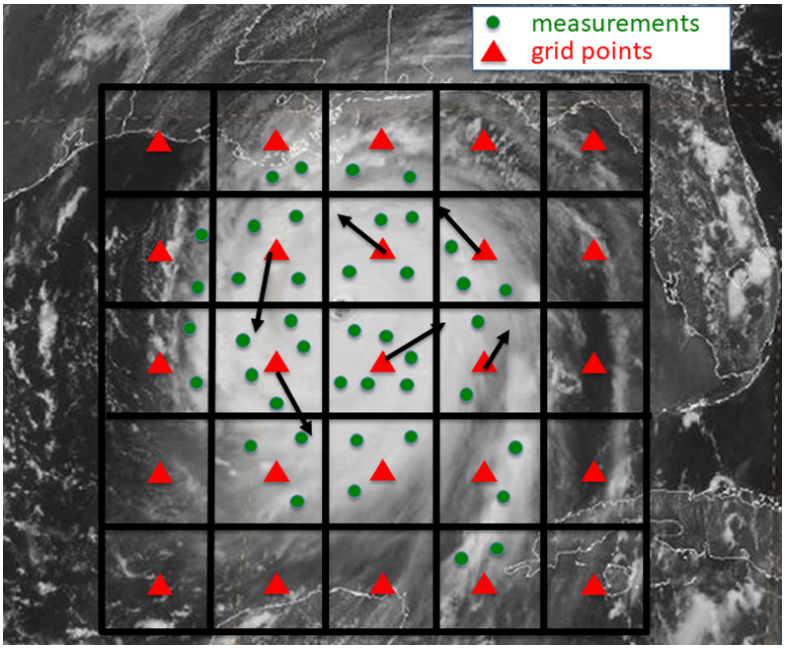

Figure 3.5: Illustration of the wind retrieval grid (red triangles) superimposed on a satellite image of a hurricane. Green dots represent available Doppler measurements. The retrieval algorithm estimates the wind vector at each grid point using nearby HLOS measurements. Source: Silva et al. (2025).

The wind retrieval is ultimately formulated as a regularized least-squares problem:

$$J(\vec{x}) = \frac{1}{2}\|A\vec{x} - \vec{b}\|^2 + \frac{\lambda^2}{2}\|D\vec{x}\|^2,$$

where $\vec{x}$ collects the wind components at all grid points, A encodes the measurement geometry, $\vec{b}$ the Doppler observations, D a finite-difference approximation of divergence, and λ is a tunable regularization parameter. A conjugate gradient solver is applied iteratively, with a multiscale strategy used to refine the solution by gradually decreasing the correlation length L.

This geometrically-aware and physically-constrained retrieval framework allows the reconstruction of the two-dimensional wind field from anisotropic and sparse HLOS observations, setting the foundation for the validation and analysis presented in the following chapter.

Chapter 4

WIVERN Performance in Observing TC Wind Structure and RI

This chapter presents a comprehensive evaluation of tropical cyclone wind fields as observed through simulated Doppler measurements from the WIVERN mission. The goal is to assess WIVERN ability to reconstruct three-dimensional wind structures and capture the key dynamical signatures associated with storm evolution, with particular emphasis on RI episodes. Through a series of retrieval experiments applied to synthetic WIVERN overpasses of Hurricane Milton, the retrieved horizontal wind vectors are compared against the reference wind fields provided by a high-resolution numerical model. The analysis spans multiple altitudes and cyclone intensities, covering both pre-intensification and post-intensification stages. In addition, the study incorporates a parametric cyclostrophic wind model to further analyze the radial structure of the storm and track the evolution of key features such as the RMW and the inner-core asymmetries. These diagnostics are used to quantify the ability of WIVERN to detect and monitor changes in the storm structure relevant to operational forecasting. Altogether, the chapter provides evidence of how WIVERN-derived wind retrievals may contribute to a better understanding of tropical cyclone dynamics and improve short-term predictions of storm intensification.

4.1 WIVERN Capability to Resolve 3D Wind Structures

4.1.1 Doppler Wind Retrieval from Simulated Overpasses

To evaluate the performance of the WIVERN mission in reconstructing the three-dimensional wind structure of tropical cyclones, this section presents results from two simulated satellite overpasses across Hurricane Milton. The selected scenes correspond to distinct stages of the storm's lifecycle, as shown in Figure 4.1: the first prior to a RI event, and the second following a significant increase in storm intensity, respectively at 00:00:00 UTC and 12:00:00 UTC on 7 October 2024, corresponding to Category 1 and Category 3 intensity. These cases provide a representative basis to assess the capability of WIVERN to retrieve horizontal wind vectors and monitor storm evolution over time. The Doppler retrieval methodology follows the approach outlined in Chapter 3, which includes gridded interpolation of model outputs, simulation of radar LOS Doppler velocities using WIVERN's scanning geometry, and the application of a geometric wind retrieval algorithm to reconstruct horizontal wind components. The analysis focuses on altitudes between 1 km and 16 km, where hydrometeor concentration ensures sufficient backscattered power for Doppler estimation.

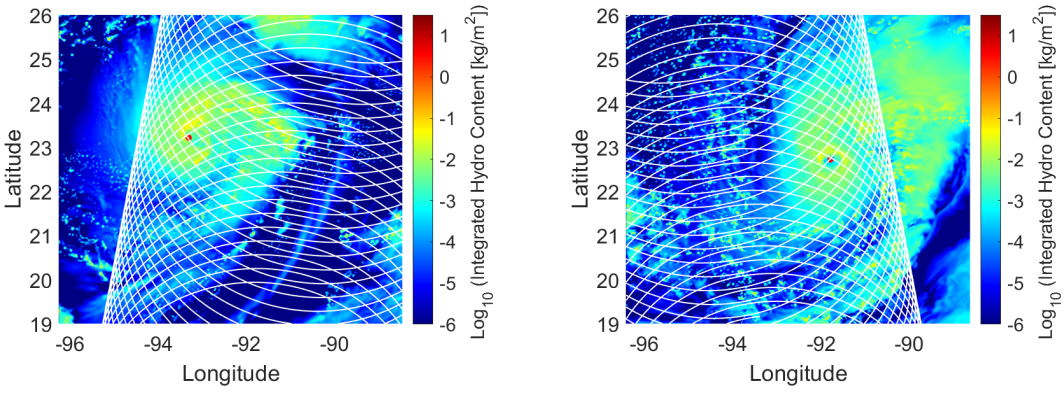

(a) 00:00 UTC – Category 1 **(b)** 12:00 UTC – Category 3

Figure 4.1: The two panels correspond to (a) before the RI event at 00:00 UTC and (b) after significant intensification at 12:00 UTC on 7 October 2024. Logarithmic maps of the integrated hydrometeor content (in kg/m^2) over the domain, derived from WIVERN-simulated observations. Red circle marks the location of TC center. WIVERN simulted scan is indicated by the white track.

A first step in the analysis concerns the hydrometeor distribution and its influence on the quality of Doppler observations. Figures 4.2 and 4.3 display the WIVERN-simulated reflectivity (Z_{measured}) and the PIA at 3, 7, 11, and 15 km altitude for the two overpasses. As expected, PIA values are most pronounced at lower levels, where radar beams traverse thicker hydrometeor-laden layers. At 15 km, PIA approaches zero across the domain, consistent with the near-complete absence of significant hydrometeor mass at such heights. The reflectivity fields reveal a clear structural evolution of the storm: during the Category 1 stage, the signal is mainly confined to fragmented convective bands, whereas in the Category 3 case, reflectivity is stronger and more spatially organized, particularly around the eyewall and major rainbands. The inner-core region during the more intense stage is characterized by high reflectivity and correspondingly elevated PIA values, especially at lower altitudes. These results align with the theoretical expectations outlined in Chapter 1, where increased hydrometeor loading and deep convection are associated with both stronger reflectivity signals and enhanced attenuation.
A detailed assessment of the wind retrieval performance is provided in Figures 4.4 and 4.5, which compare model winds and retrieved winds at 3 km, 7 km, 11 km, and 15 km. Each row corresponds to a different altitude, while the columns show, respectively, the model wind field, the WIVERN-retrieved field, and the absolute error between the two. The retrieval proves capable of reconstructing the large-scale cyclonic circulation across all levels, with particularly good agreement at mid-altitudes (6–10 km), where the Doppler signal is stronger and less affected by vertical motions. Discrepancies are mainly concentrated near the eye and within convective towers, where sharp reflectivity gradients and attenuation reduce retrieval accuracy. At higher intensity (Category 3), increased asymmetry in the wind field is observed, but the retrieval remains able to capture the main circulation features and the radial structure with reasonable fidelity.

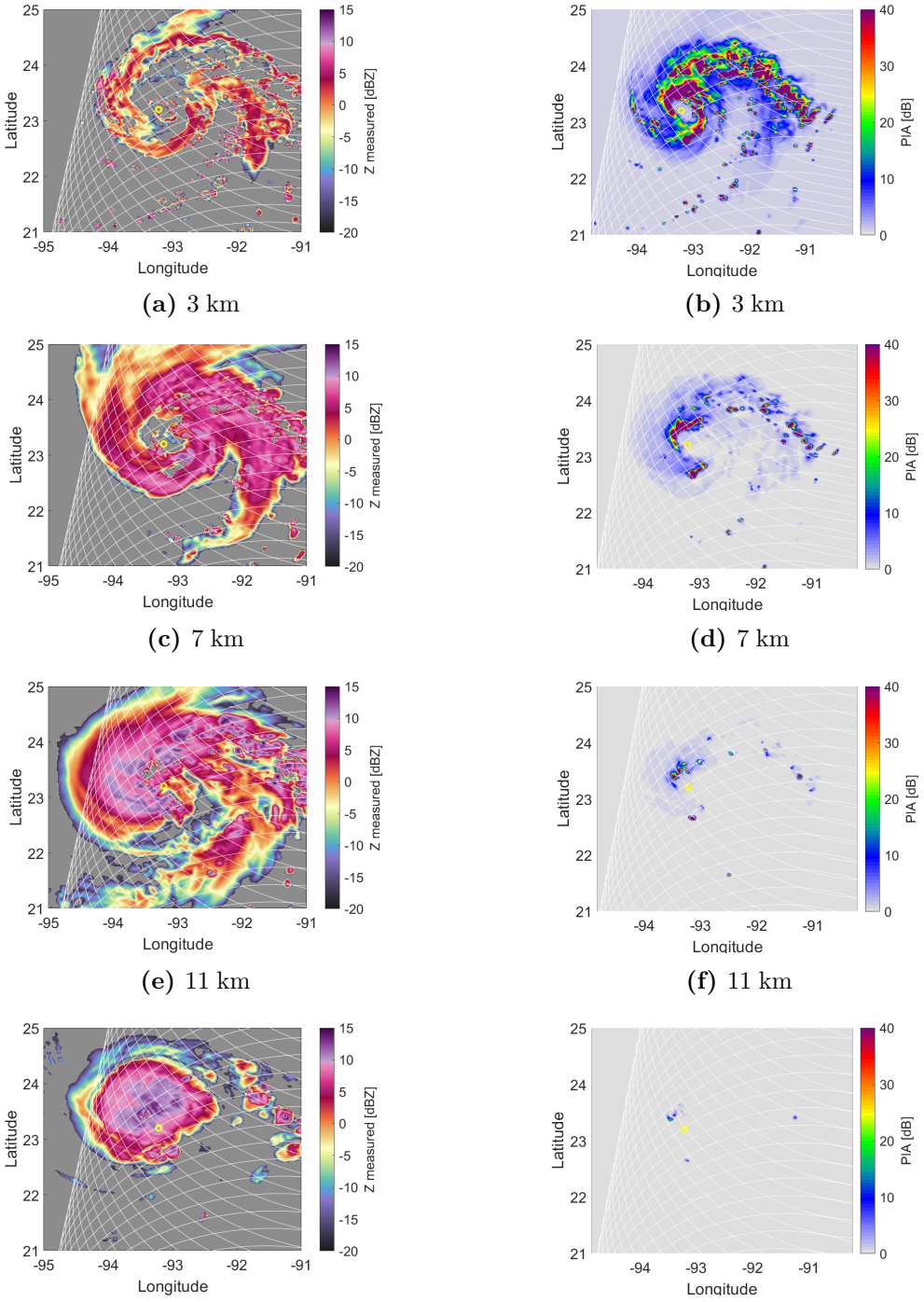

(a) 3 km **(b)** 3 km

(c) 7 km **(d)** 7 km

(e) 11 km **(f)** 11 km

(g) 15 km **(h)** 15 km

Figure 4.2: WIVERN-simulated Z_{measured} and PIA at different altitudes for Hurricane Milton at CAT 1.

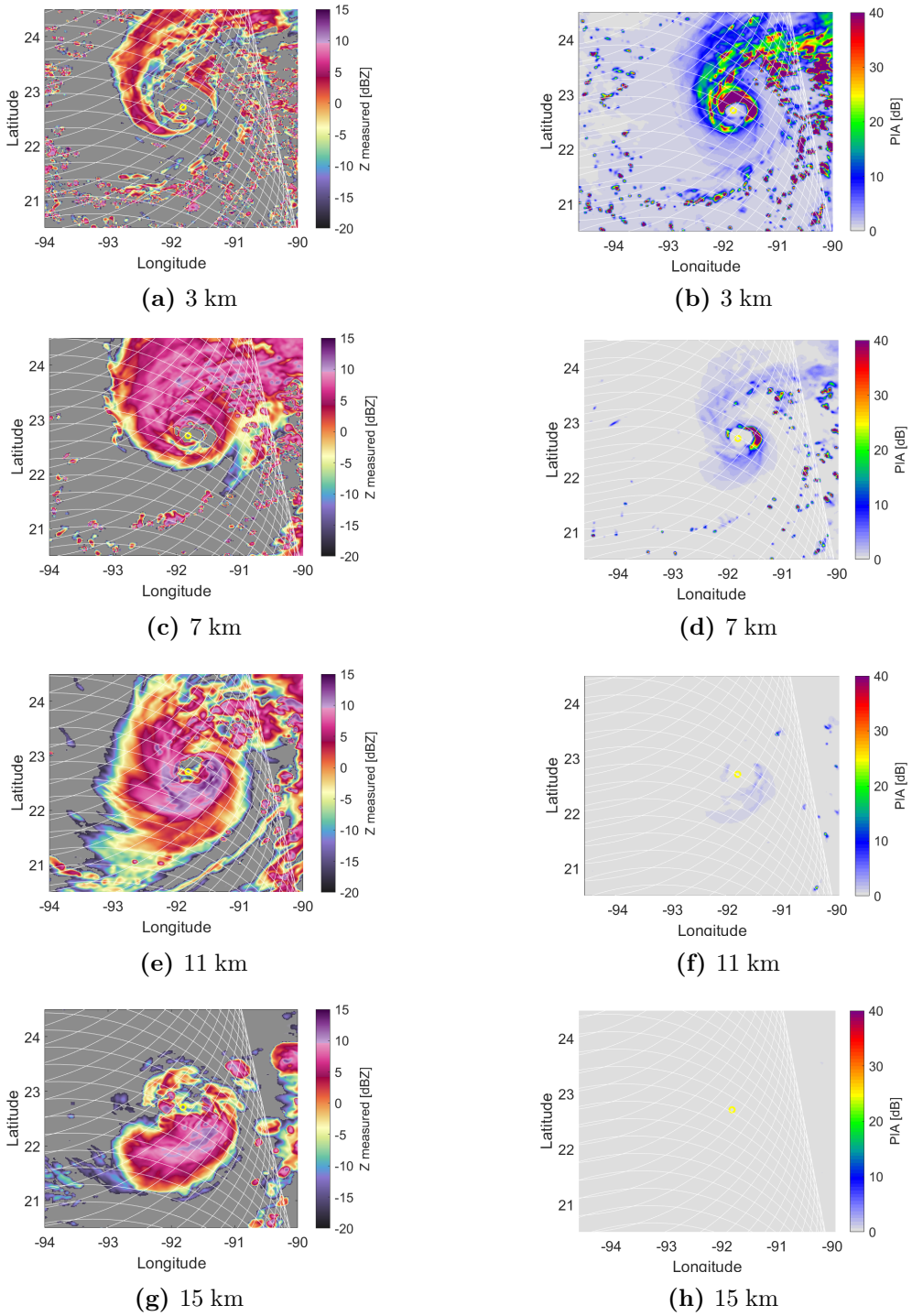

(a) 3 km **(b)** 3 km

(c) 7 km **(d)** 7 km

(e) 11 km **(f)** 11 km

(g) 15 km **(h)** 15 km

Figure 4.3: WIVERN-simulated Z_{measured} and PIA at different altitudes for Hurricane Milton at CAT 3.

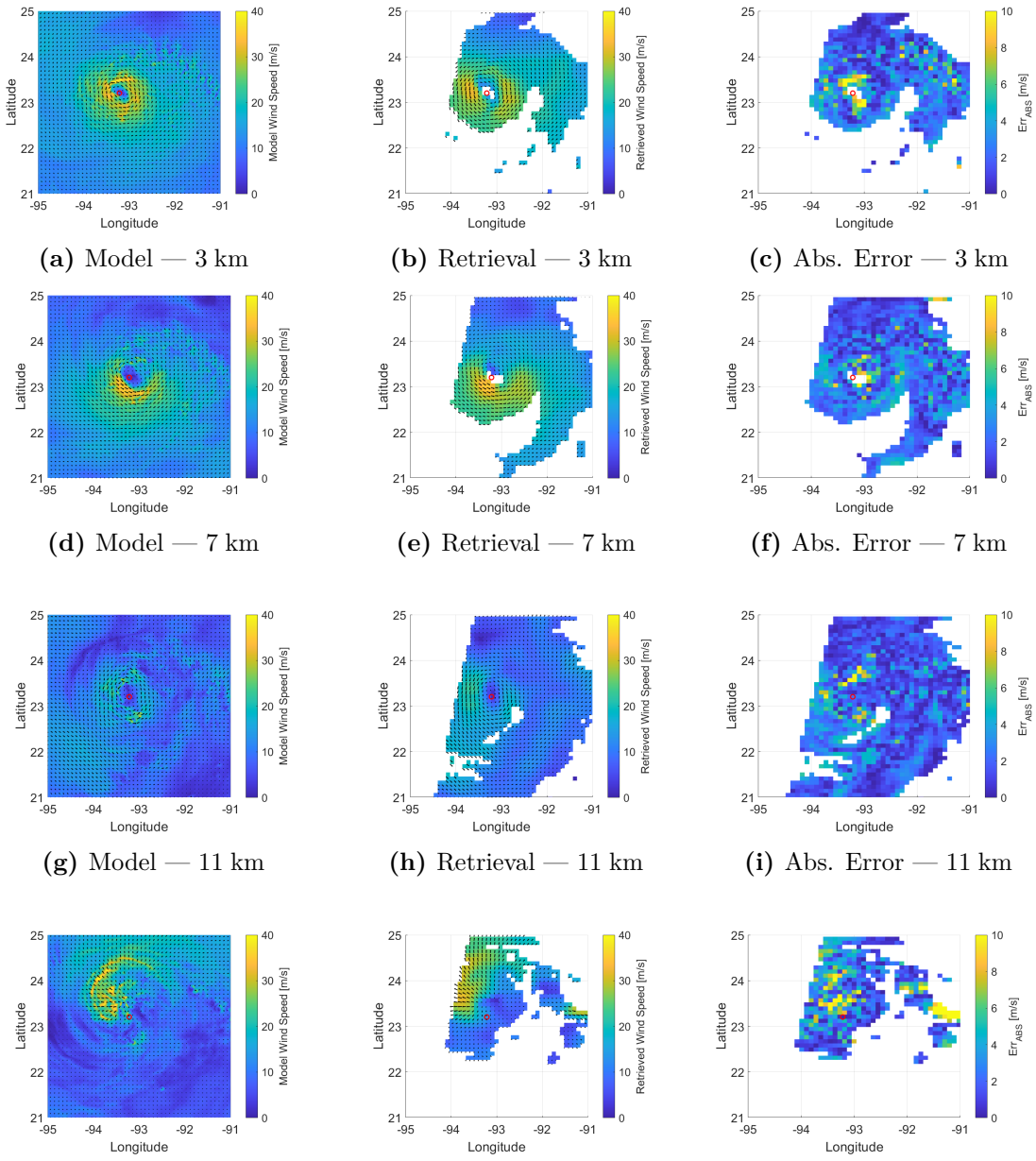

(a) Model — 3 km **(b)** Retrieval — 3 km **(c)** Abs. Error — 3 km

(d) Model — 7 km **(e)** Retrieval — 7 km **(f)** Abs. Error — 7 km

(g) Model — 11 km **(h)** Retrieval — 11 km **(i)** Abs. Error — 11 km

(j) Model — 15 km **(k)** Retrieval — 15 km **(l)** Abs. Error — 15 km

Figure 4.4: Wind retrieval results at different altitudes (3, 7, 11, 15 km) for Hurricane Milton at 00:00:00 UTC, 7 October 2024. Each row shows the model wind field, the retrieved field, and the absolute error.

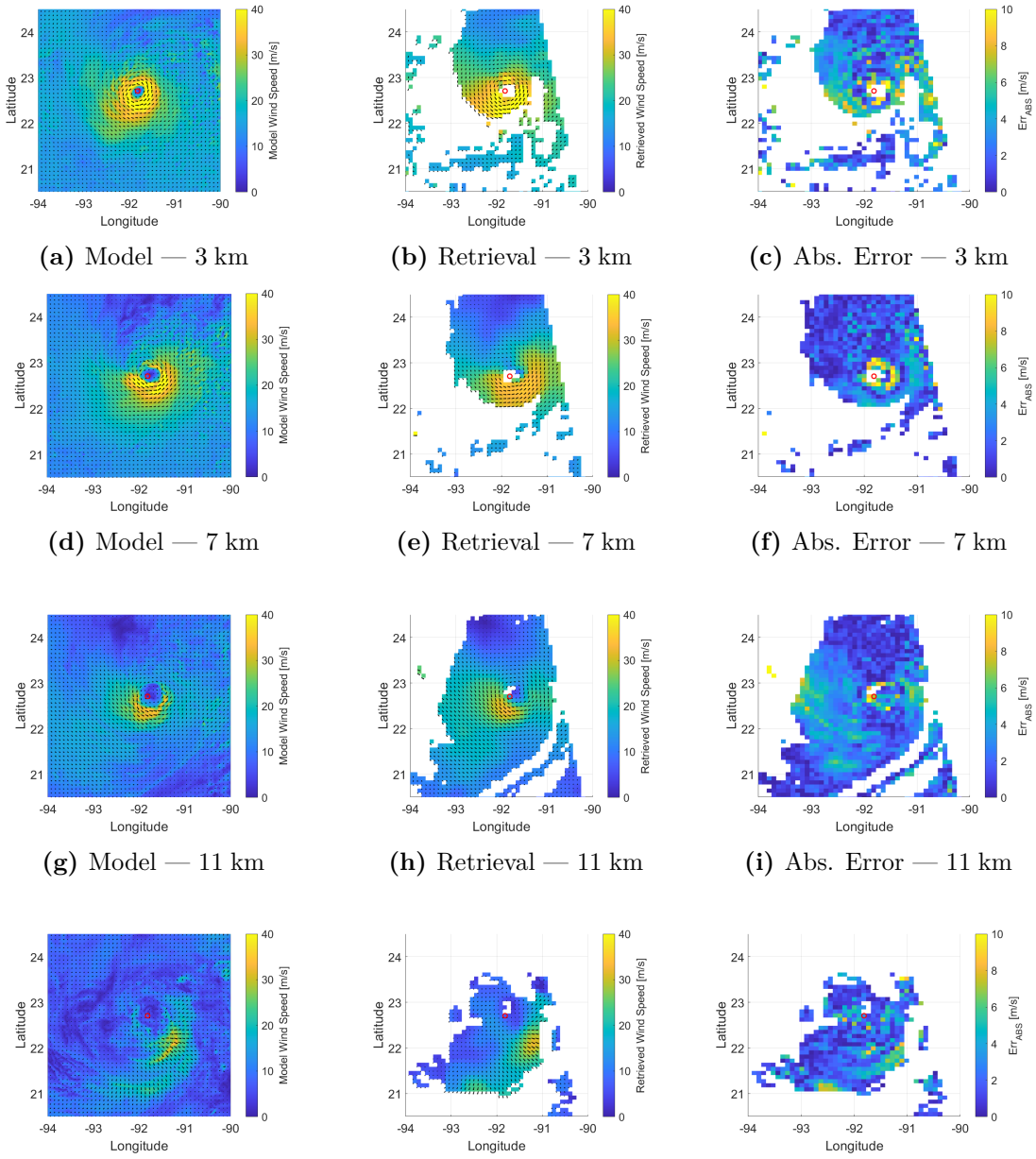

(a) Model — 3 km **(b)** Retrieval — 3 km **(c)** Abs. Error — 3 km

(d) Model — 7 km **(e)** Retrieval — 7 km **(f)** Abs. Error — 7 km

(g) Model — 11 km **(h)** Retrieval — 11 km **(i)** Abs. Error — 11 km

(j) Model — 15 km **(k)** Retrieval — 15 km **(l)** Abs. Error — 15 km

Figure 4.5: Wind retrieval results at different altitudes (3, 7, 11, 15 km) for Hurricane Milton at 12:00:00 UTC, 7 October 2024. Each row shows the model wind field, the retrieved field, and the absolute error.

4.1.2 Inflow Structures in the Lower Troposphere

As discussed in Chapter 2, the lowermost levels of a tropical cyclone are dominated by strong radial inflow, where air parcels spiral inward toward the cyclone center. This inward transport of angular momentum is crucial to supporting the cyclone's convective structure and sustaining intensification (Montgomery et al. 2006). To assess WIVERN capability to retrieve this inflow structure, Figure 4.6 presents retrieved horizontal wind vectors projected along the radial direction. The analysis is shown for three altitudes: 1, 2, and 3 km. These levels fall within the boundary layer, where the radial component of the wind is typically strongest. In the figures, the background shading represents the magnitude of the model-simulated radial wind, while the black arrows show the model's radial wind vectors, and the red arrows depict those retrieved from WIVERN. The wind vectors are computed with respect to the estimated storm center and projected onto the local radial axis. According to the adopted convention, negative radial wind indicates inflow (toward the cyclone center), while positive values represent outflow (away from the center). These plots illustrate the evolution of the near-surface radial circulation before and after the rapid intensification phase. A qualitative comparison between the two intensity stages reveals a clearer and more structured inflow at low levels in the Category 3 case, consistent with the expected intensification of the boundary layer circulation. In contrast, the Category 1 stage exhibits a weaker and less organized inflow pattern. These results are in line with theoretical expectations, where stronger storms are typically associated with more focused and sustained low-level inflow feeding the eyewall convection.

4.1.3 Upper-Tropospheric Divergence

In the upper troposphere, tropical cyclones are characterized by divergent outflow that radiates outward from the storm center. This outflow, typically found above 13 km, plays a key role in venting rising air from the convective core and sustaining vertical development. At 14 to 16 km altitude, WIVERN retrievals show a well-defined divergent flow around the storm center, broadly consistent with the model fields. Figure 4.7 shows the radial wind vectors retrieved at 14, 15, and 16 km altitude for the Category 1 and Category 3 overpasses, respectively. In both cases, the retrieved wind vectors reproduce the broad divergent flow aloft, confirming the theoretical link between strong outflow and tropical cyclone development. As the storm strengthens, the outflow becomes more pronounced and spatially extended, in line with the enhanced ventilation mechanisms described in Chapter 2.

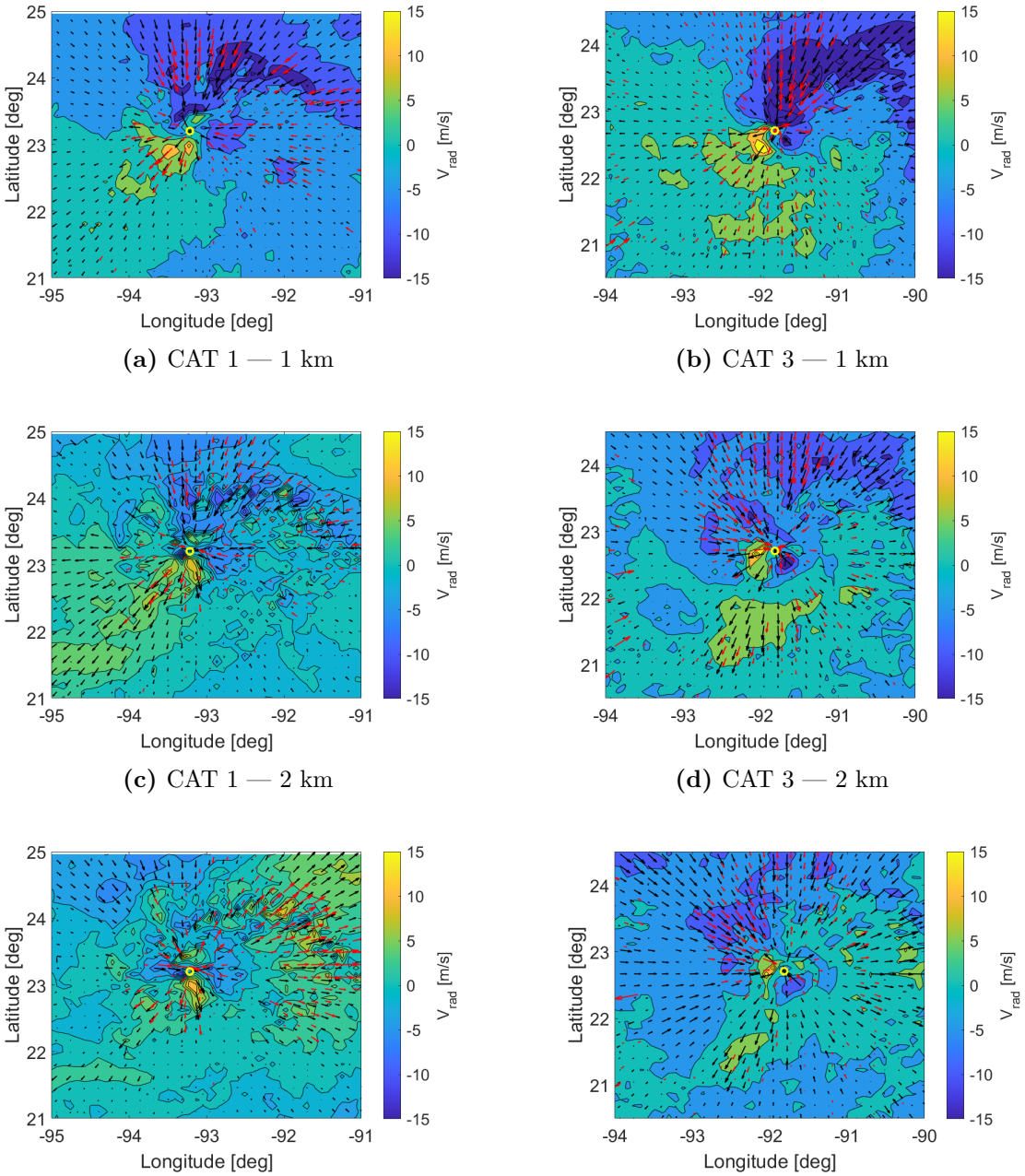

(a) CAT 1 — 1 km

(b) CAT 3 — 1 km

(c) CAT 1 — 2 km

(d) CAT 3 — 2 km

(e) CAT 1 — 3 km

(f) CAT 3 — 3 km

Figure 4.6: Model (balck vectors) and retrieved (red ones) radial wind vectors at 1, 2, and 3 km altitude during the WIVERN overpasses on Hurricane Milton. Left column: Category 1 at 00:00 UTC; right column: Category 3 at 12:00 UTC on 07 October 2024.

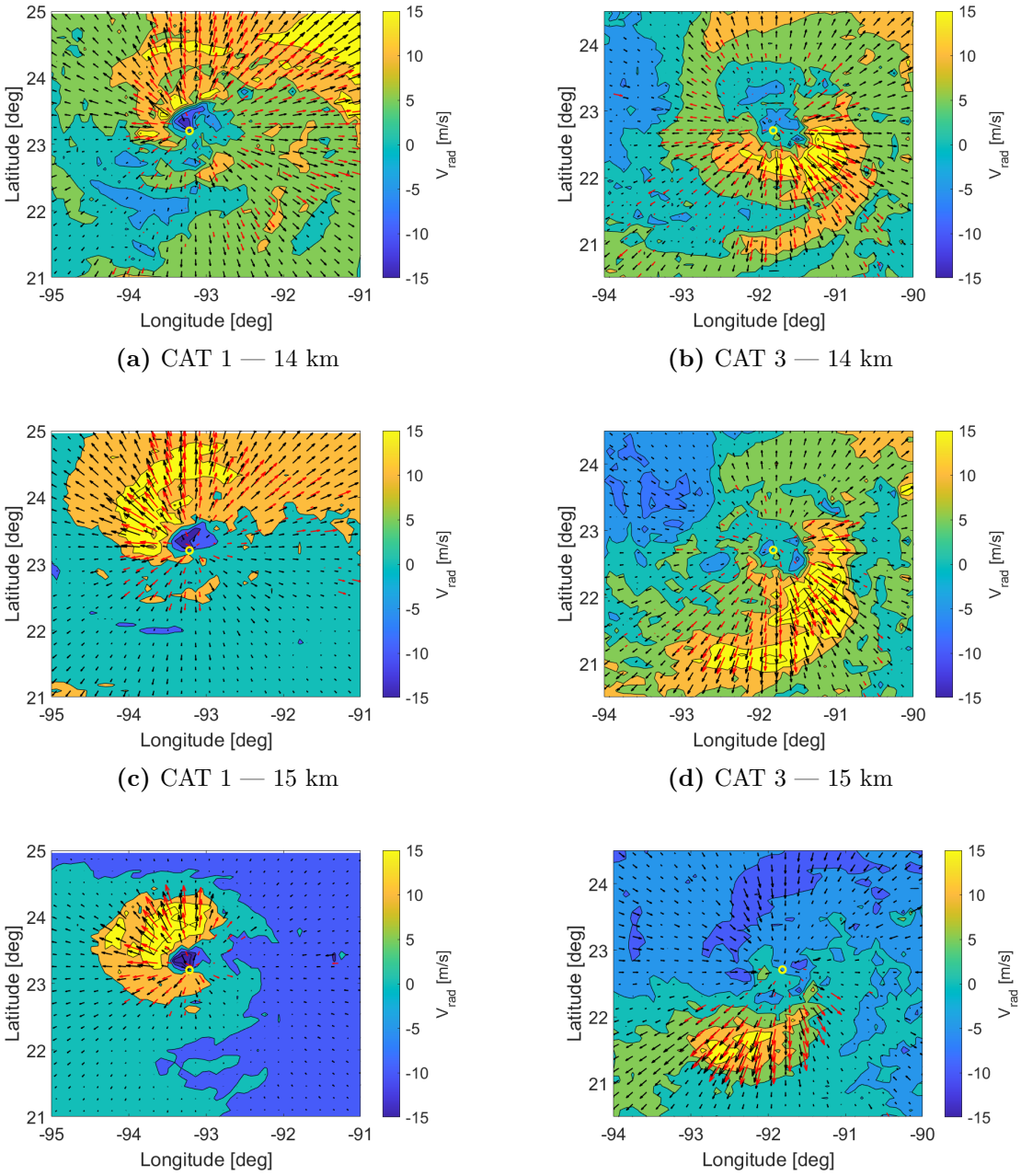

(a) CAT 1 — 14 km

(b) CAT 3 — 14 km

(c) CAT 1 — 15 km

(d) CAT 3 — 15 km

(e) CAT 1 — 16 km

(f) CAT 3 — 16 km

Figure 4.7: Same as Figure 4.6, but for upper-level altitudes (14–16 km).

4.1.4 Environmental Shear–Quadrant Analysis and TC Asymmetries

Environmental vertical wind shear is a key large-scale factor known to influence TC structure and intensification. Defined as the vector difference between horizontal winds at upper and lower tropospheric levels, typically between 200 and 850 hPa, shear has the potential to disrupt the vertical alignment of the vortex, favoring the development of structural asymmetries in convection, inflow, and outflow patterns (Frank and Ritchie 2001; Rogers, Reasor, et al. 2013). In low-shear conditions, convection tends to remain symmetrically organized around the storm center, allowing efficient vertical coupling and latent heat release, which supports intensification. Conversely, moderate-to-strong shear may tilt the vortex and displace convection downshear, inhibiting intensification or even causing weakening (Houze 2010).

However, observational and modeling studies (Rogers, Reasor, et al. 2013; Wu et al. 2016) have demonstrated that asymmetric structures can still organize and persist under moderate shear, especially when aided by strong convective bursts and coherent inflow. The WIVERN mission has been specifically designed to capture these features, offering, for the first time from space, a three-dimensional reconstruction of in-cloud horizontal winds with sufficient spatial coverage and resolution to observe such asymmetries, even in the glaciated upper troposphere and near the storm core.

To further investigate the internal asymmetries in the storm structure, a qualitative shear-relative quadrant division was introduced, based on the direction of the environmental vertical wind shear. The shear vector was computed as the difference between the 200 and 850 hPa horizontal winds, averaged over a 200-600 km annulus surrounding the cyclone center. This yielded a reference orientation with respect to which the storm was divided into four shear-relative quadrants: downshear right (DR), downshear left (DL), upshear left (UL), and upshear right (UR), as shown in Figure 4.8.

While this decomposition is not used here for quantitative dynamic interpretation, it provides a useful framework to highlight WIVERN capability to resolve internal storm asymmetries. Even under moderate shear, the retrieved wind vectors show distinct patterns of low-level inflow and upper-level divergence that vary with quadrant. Identifying these quadrant-dependent structures is important for several reasons: it enables a more physically consistent initialization of high-resolution numerical models, helps validate the performance of convective-scale simulations, and supports the interpretation of convective organization under varying environmental forcing.

The use of quadrant-based analysis in the context of tropical cyclones has been widely adopted in both observational and modeling studies (DeHart et al. 2014;

Rogers, Reasor, et al. 2013; Matyas 2010). Recently, A. Battaglia, Recupero, et al. (2025) emphasized its importance for spaceborne Doppler radars, noting that the ability to detect spatially coherent asymmetries in the inner core, even in sheared environments, is essential for studying convective bursts, vortex tilt, and storm evolution. WIVERN, with its global coverage and high-resolution wind retrievals, offers a new opportunity to routinely identify and monitor these features from space.

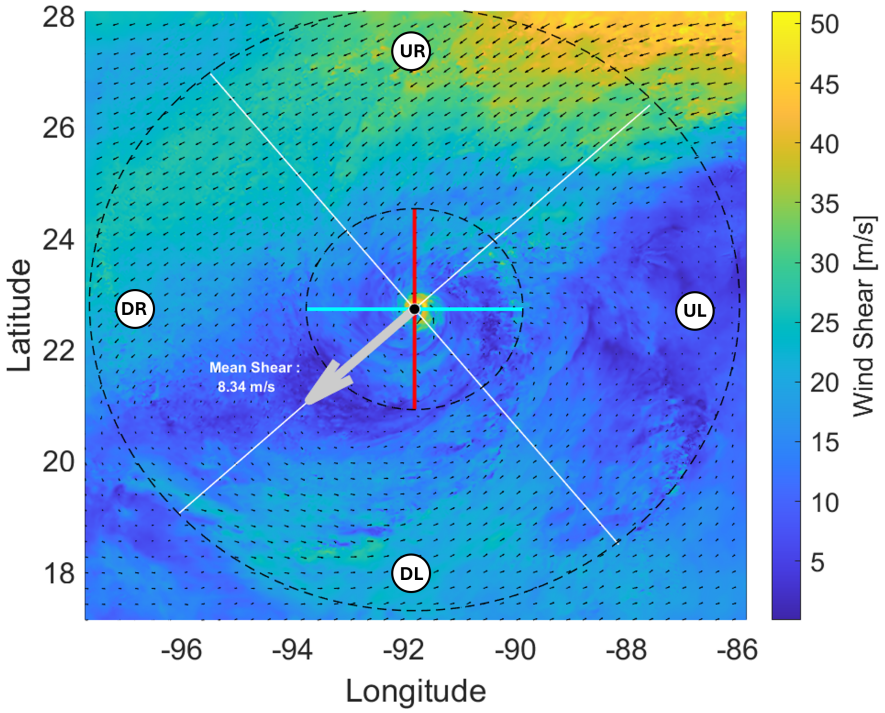

Figure 4.8: Shear-relative quadrant division for Hurricane Milton on 07 October 2024 at 12:00 UTC. The gray arrow shows the environmental shear vector; white lines separate the four quadrants (DR, DL, UR, UL). The dashed circles (200-600 km) define the annulus used for computing the shear vector.

In addition to horizontal wind retrievals, WIVERN provides co-located reflectivity measurements that offer valuable insight into the three-dimensional structure of tropical cyclones. In this study, two vertical cross-sections were extracted through the eye of Hurricane Milton: a meridional slice along the 0°-180° azimuth (intersecting the downshear-left to upshear-right quadrants) and a zonal slice along 90°-270° (from downshear-right to upshear-left), selected to capture asymmetries relative to the environmental shear direction (see Figure 4.8). Each cross-section is presented using two complementary visualizations. The first highlights the modeled radial and vertical wind field using a color map, overlaid with black arrows to depict horizontal

radial wind vectors. The second panel displays the reflectivity field as measured by WIVERN, overlaid with radial wind vectors from both the model (black arrows) and WIVERN retrievals (white arrows). Semi-transparent thick arrows indicate the broader-scale circulation patterns. Superimposed green and blue contours represent vertical motions, specifically updrafts stronger than +3 m/s and downdrafts weaker than −1 m/s, respectively. This multi-variable representation allows a detailed view of the storm's internal dynamics, emphasizing coherent inflow pathways, deep convective updrafts near the eyewall, and ventilation processes at upper levels. This layout enables a direct comparison between observed microphysical structures and the reconstructed wind field. The reflectivity cross-sections reveal several key features of the inner core, including a well-defined eye, evident as a central region of near-zero reflectivity, surrounded by a sharply bounded eyewall exhibiting strong horizontal reflectivity gradients. In multiple locations, particularly on the lower sides of the convective towers of the eyewall, the reflectivity signal shows localized attenuation, with values dropping below detection threshold. These reflectivity minima are evidence of strong hydrometeor attenuation and possible W-band extinction caused by high concentrations of liquid and frozen particles such as graupel or rain. Thanks to its off-nadir scanning geometry, WIVERN is capable of capturing these signatures with greater continuity and angular diversity than traditional nadir-looking radar systems. Overall, the ability to resolve such fine-scale vertical structures, ranging from deep convection and organized updrafts to the morphology of the eye and localized attenuation regions, demonstrates WIVERN unique potential to characterize both the dynamical and microphysical evolution of tropical cyclones. When combined with the quadrant-based interpretation of the wind field, these reflectivity observations contribute to a comprehensive and physically consistent depiction of storm structure, with direct relevance for forecasting, process studies, and assimilation into numerical models.

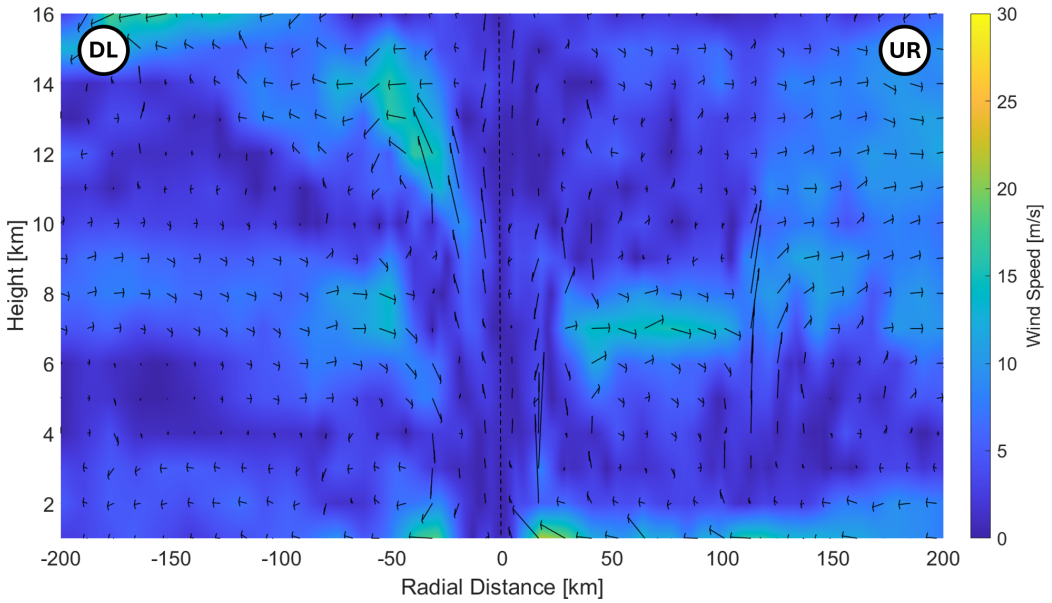

(a) Cross-section of model wind speed and direction across the 0°–180° diameter (downshear left to upshear right).

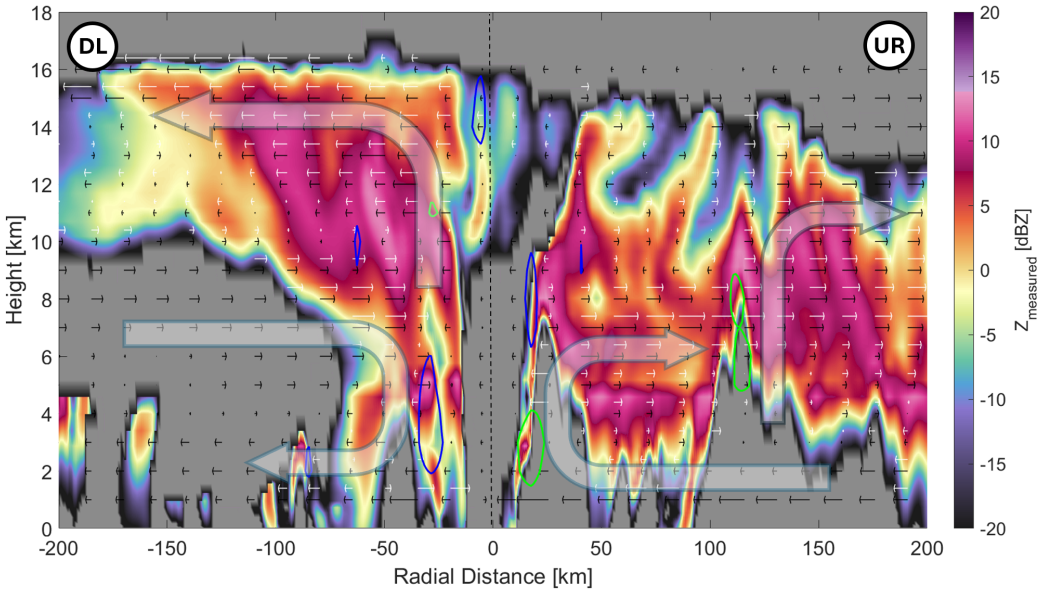

(b) Corresponding WIVERN reflectivity field with model (black) and retrieved (white) radial wind vectors.

Figure 4.9: Vertical cross-sections through Hurricane Milton along the 0°–180° axis at 12:00 UTC on 10 July 2024. The direction corresponds to the downshear left–upshear right quadrants, as defined in Figure 4.8.

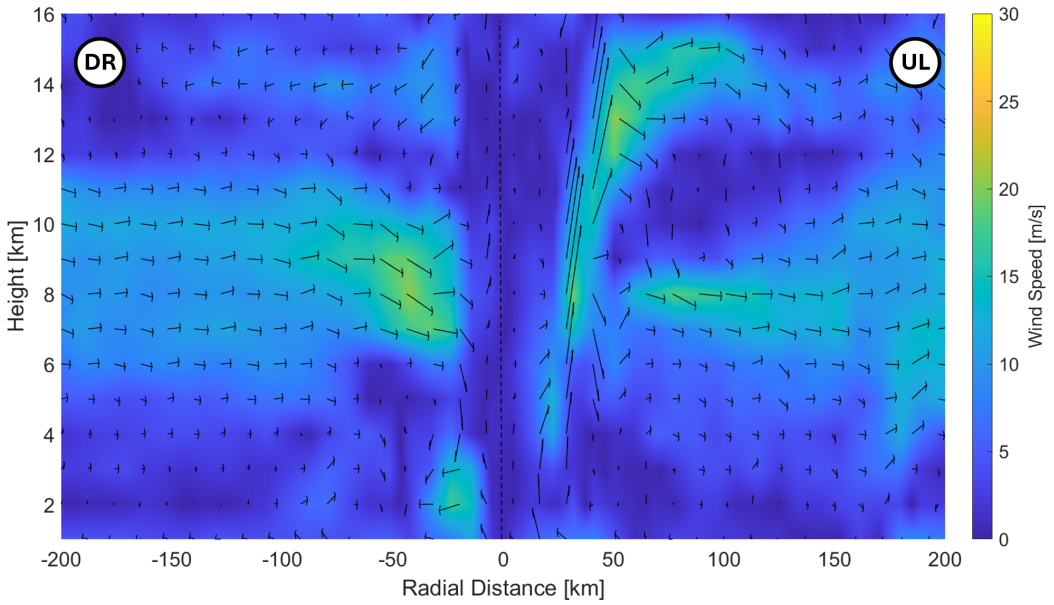

(a) Cross-section of model wind speed and direction across the 90°–270° diameter (downshear right to upshear left).

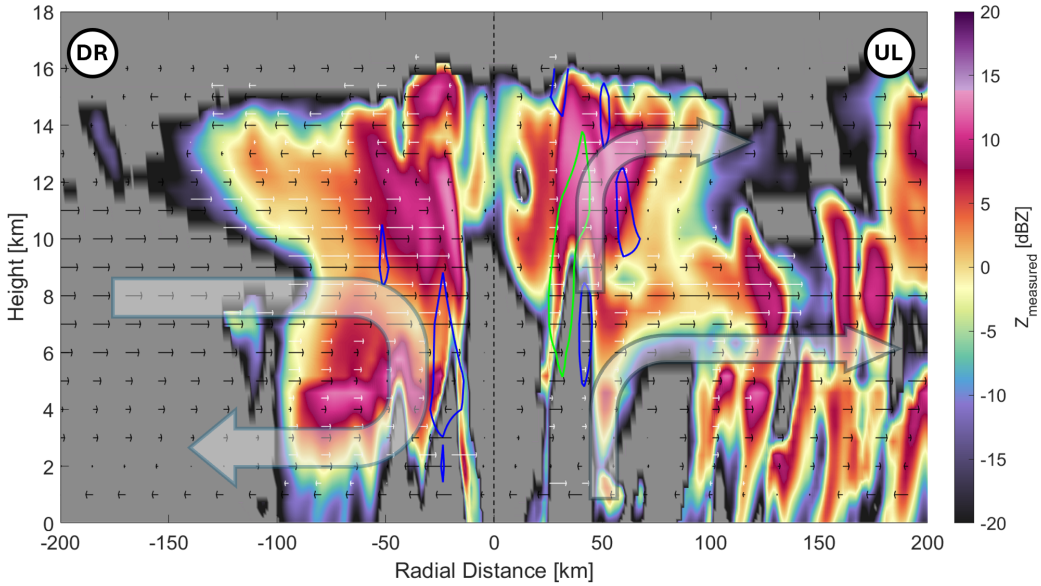

(b) Corresponding WIVERN reflectivity field with model (black) and retrieved (white) radial wind vectors.

Figure 4.10: Vertical cross-sections through Hurricane Milton along the 90°–270° axis at 12:00 UTC on 10 July 2024. The direction corresponds to the downshear right–upshear left quadrants, as defined in Figure 4.8.

4.2 Monitoring TC Intensification Through Inner-Core Wind Estimates

The results presented in this section are particularly relevant in the context of Rapid Intensification, a process that critically depends on the structure and dynamics of the inner core. As discussed in Chapter 2, identifying asymmetries in the low-level inflow and upper-level outflow, as well as monitoring convective bursts near the eyewall, can serve as precursors to RI. The ability of WIVERN to resolve the inner-core wind field with fine spatial detail is therefore crucial for capturing such structural features, enabling early detection of intensification signals.

4.2.1 Cyclostrophic Wind Modeling: The Holland (1980) Profile

To interpret the observed structure of inner-core winds and relate it to theoretical expectations, the cyclostrophic wind profile proposed by Holland (1980) is used in this study as a reference. This semi-empirical model provides a parametric, axisymmetric representation of the radial distribution of tangential wind and pressure in tropical cyclones. It is based on the assumption of cyclostrophic balance, valid in the inner-core region where the centrifugal force dominates over the Coriolis force.

The pressure profile in the Holland model is given by:

$$P(r) = P_c + (P_n - P_c) \exp\left[-\left(\frac{RMW}{r}\right)^B\right],$$

where: - $P(r)$ is the pressure at radius r, - P_c is the central pressure, - P_n is the environmental pressure, - RMW is the radius of maximum wind, - B is a dimensionless shape parameter that controls the sharpness of the pressure gradient.

From the pressure gradient and assuming cyclostrophic balance, the tangential wind profile becomes:

$$V(r) = V_{\max}\left(\frac{RMW}{r}\right)^B \exp\left[1 - \left(\frac{RMW}{r}\right)^B\right],$$

where $V_{\max}$ is the maximum wind speed at RMW. This equation captures the rapid increase of tangential wind speed near the eyewall and its exponential decay outward. The parameter B is critical: higher values yield narrower, more peaked wind profiles; lower values indicate broader wind distributions, as presented in Figure 4.11.

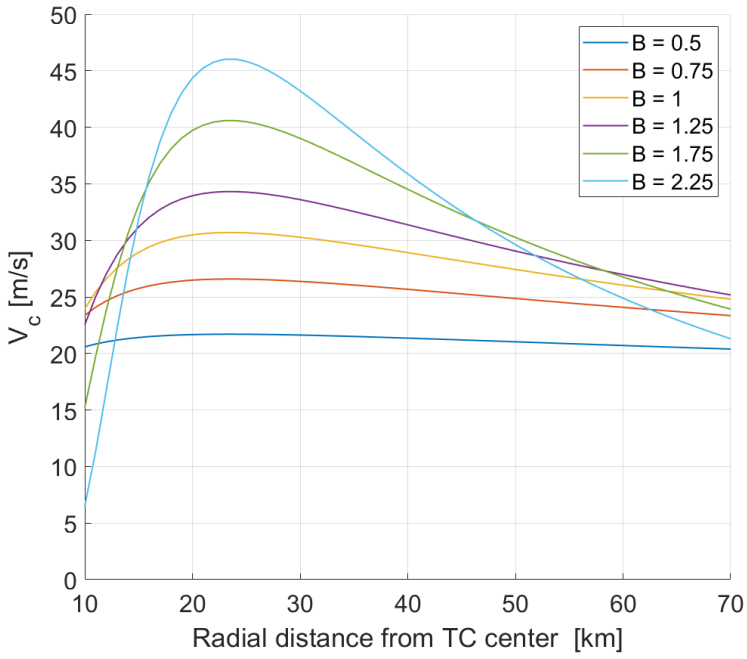

Figure 4.11: Tangential wind profiles generated using the Holland model, illustrating the influence of the shape parameter B.

Due to its simplicity and flexibility, the Holland model has been widely adopted in both operational forecasting and research. It requires only a few storm parameters and offers a smooth, continuous profile that can be fitted to observational or model data. Its structure makes it especially suitable for diagnosing inner-core wind characteristics and their evolution during rapid intensification. However, the model also presents some limitations. It assumes a symmetric storm structure and does not account for environmental vertical wind shear or asymmetric convective features. As such, it may not capture localized anomalies or quadrant-dependent variations. Nonetheless, it remains a valuable baseline for comparison, particularly in the context of satellite-based wind retrievals such as those provided by WIVERN.

In the following section, the Holland model is applied to both model-simulated and WIVERN-retrieved radial wind profiles of Hurricane Milton, spanning intensities from Category 1 to Category 5. The goal is to assess how closely the observed wind structure approximates an idealized, symmetric profile.

4.2.2 Application of the Holland Model to WIVERN and Model Data

To assess the capability of WIVERN to capture the radial structure of the wind field during rapid intensification, the Holland (1980) wind profile was fitted to both model output and WIVERN-retrieved data for two overpasses of Hurricane Milton: the Category 1 stage (07 October 2024 at 00:00 UTC) and the Category 5 stage (08 October 2024 at 00:00 UTC), as presented in Figure 4.12. For each case, the tangential wind was extracted along radial cross-sections centered on the estimated cyclone center. From the 2D wind fields, the tangential component was computed with respect to the local radius, and a mean radial profile was obtained by averaging over a narrow azimuthal sector near the direction of maximum wind. The analysis focused on the lower troposphere, precisely at 2 km altitude, where the cyclostrophic approximation is most valid and where the peak winds are typically located.

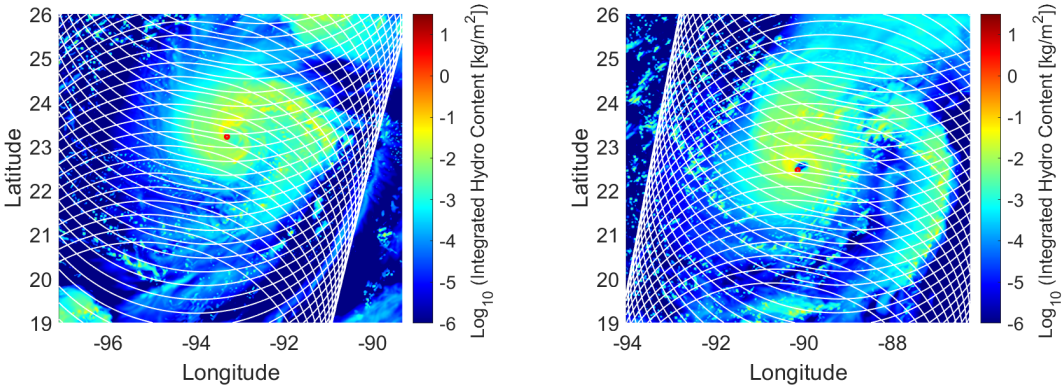

(a) Category 1 **(b)** Category 5

Figure 4.12: The two panels correspond to (a) before the RI event at 00:00 UTC on 7 October 2024 and (b) after significant intensification at 00:00 UTC on 8 October 2024. Logarithmic maps of the integrated hydrometeor content (in kg/m^2) over the domain, derived from WIVERN-simulated observations. Red circle marks the location of TC center. WIVERN simulted passage is indicated by the white track.

Before applying the Holland model, it is instructive to examine the structure of the horizontal wind field to evaluate the validity of the cyclostrophic approximation, which assumes that the tangential wind component dominates over the radial one in the force balance. Figure 4.13 shows the tangential and radial wind components at 2 km altitude for both the Category 1 and Category 5 stages of Hurricane Milton, as derived from model simulations. The plots reveal clear structural differences between the two stages. In the Category 5 case, the tangential wind field is highly

organized and displays a strong, azimuthally coherent circulation within the inner core, delineated by the white 70 km radius circle in the plots. In contrast, the radial wind component remains relatively weak and spatially confined, supporting the assumption that centrifugal forces dominate over radial inflow or outflow. This configuration aligns with the idealized conditions under which cyclostrophic balance is considered valid. In the Category 1 case, however, the tangential wind is less intense and more irregularly distributed, while the radial component exhibits stronger relative contributions, particularly in the outer portions of the inner core. These characteristics suggest a less organized vortex structure, potentially influenced by environmental shear, and indicate that the cyclostrophic approximation may be less strictly applicable under weaker storm conditions. Nevertheless, since the Holland model is designed as a symmetric, idealized baseline, and considering that wind retrievals are subject to spatial sampling limitations, the approximation remains valuable. It provides a useful reference framework for evaluating first-order structural consistency and for comparing the radial organization of the wind field across different intensity stages using both model output and WIVERN-derived data.

To apply the Holland model to the wind field of Hurricane Milton, the fitting procedure was first conducted using model-derived wind speed profiles at 2 km altitude. The analysis began by identifying the RMW and the peak wind speed ($V_{\max}$) within the inner core, followed by the estimation of the corresponding surface pressure drop $\Delta P = P_n - P_c$, where P_n and P_c represent the environmental and central pressures, respectively. These parameters provided an initial estimate of the shape parameter B, according to the analytic form of the Holland wind equation. The wind profiles used for fitting were constructed from the horizontal wind module, computed as the magnitude of the vector sum of the zonal and meridional wind components. This field was then averaged over concentric radial bins centered on the estimated TC center position. The domain was divided into 1-km-wide annular rings, extending from 10 km out to 70 km, thereby encompassing the storm's inner-core region. For each radial bin, the mean wind speed was computed from all valid grid points within the respective annulus. This averaging procedure produced a smooth, two-dimensional field of mean wind speed as a function of radius. The extracted profile was used as the reference for fitting the Holland function. This method helps to suppress small-scale variability and local asymmetries, yielding a radially symmetric representation suitable for comparison with the idealized model.

To improve the fit, a two-stage optimization was performed. First, a grid search over a broad range of physically plausible parameters (B, RMW, and ΔP) was carried out by minimizing the squared error J between the observed and modeled wind profiles with Holland's function. This step yielded an initial parameter set that was subsequently refined using nonlinear least-squares optimization methods. Tables 4.1 and 4.2 summarize the optimized parameters obtained from the fitting

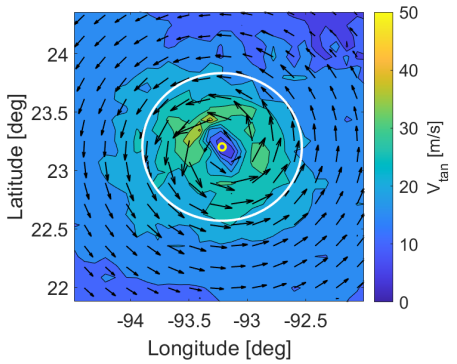

(a) Tangential wind — CAT 1

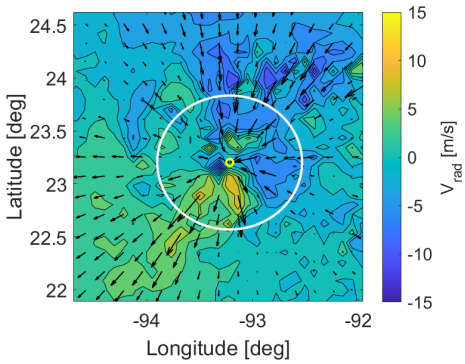

(b) Radial wind — CAT 1

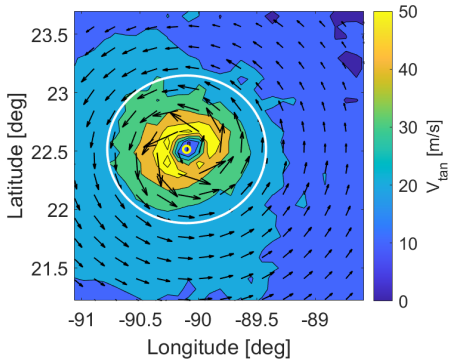

(c) Tangential wind — CAT 5

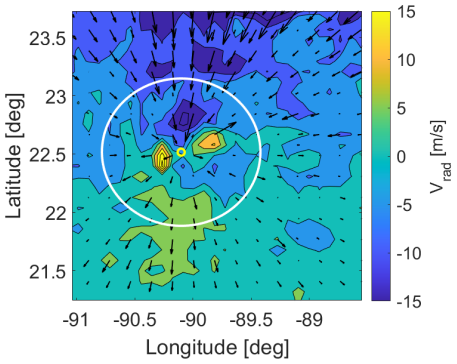

(d) Radial wind — CAT 5

Figure 4.13: Comparison of tangential (left) and radial (right) wind components at 2 km altitude for Hurricane Milton during Category 1 (top row) and Category 5 (bottom row) stages. The background shows contour maps of wind speed magnitude for the corresponding component (tangential or radial), with black arrows indicating horizontal wind vectors from the model. The white circle marks the 70 km radius around the cyclone center, used to define the inner core region.

of the Holland wind profile to the model-derived wind data at 2 km altitude. The table reports both the initial estimates derived from grid search (minimization of the squared error J) and the final values refined through nonlinear least-squares optimization using Matlab's function `lsqcurvefit`.

The same fitting methodology was applied to the WIVERN-retrieved wind data, using line-of-sight Doppler measurements corrected for platform motion and viewing geometry. Specifically, the Doppler velocity was adjusted for the atmospheric motion and projected along the local radial direction using the known

Table 4.1: Fitted parameters of the Holland model using model-derived wind profiles at 2 km altitude during the Category 1 stage (07 October 2024, 00:00 UTC). The initial guess was obtained by minimizing the squared error function J over a parameter grid. Final values were refined using nonlinear least-squares optimization (`lsqcurvefit`).

Method	**B**	**RMW** [km]	**ΔP** [Pa]
Initial guess (from J min)	1.50	25.00	1850.00
Nonlinear opt. (`lsqcurvefit`)	1.51	25.10	1847.07

Table 4.2: Fitted parameters of the Holland model using model-derived wind profiles at 2 km altitude during the Category 5 stage (08 October 2024, 00:00 UTC).

Method	**B**	**RMW** [km]	**ΔP** [Pa]
Initial guess (from J min)	2.00	20.00	4050.00
Nonlinear opt. (`lsqcurvefit`)	2.06	18.73	4226.85

off-nadir viewing angle ($\theta = 42°$). After correction, the resulting horizontal line-of-sight wind speed (V_{hlos}) was used to construct a radial wind profile. To ensure data quality, several filtering criteria were applied. Measurements were excluded if they presented reflectivity values below -18 dBZ, vertical atmospheric motion exceeding ± 2 m/s, or signal-to-clutter ratio (SCR) above a defined threshold. The filtered data were then spatially restricted to a radial annulus extending from 10 to 70 km around the estimated cyclone center, to match the region used for model fitting and to avoid central beam-filling issues. Figures 4.14 and 4.15 illustrate the evolution of the inner-core structure of Hurricane Milton before and after rapid intensification, as observed from WIVERN simulations at 2 km altitude. Figure 4.14 presents, from top to bottom, the antenna scan track superimposed on the horizontal wind speed field, and a zoomed-in view of the inner 70 km radius around the storm center. The left column refers to the Category 1 stage, and the right column to the Category 5 overpass. In the zoomed panels, blue circles represent valid Doppler measurements, while white and black crosses indicate data discarded due to low reflectivity ($Z < -18$ dBZ) or excessive vertical velocity ($|w| > 2$ m/s), respectively. Figure 4.15 shows the corresponding reflectivity fields (Z_{measured}, top row) and path-integrated attenuation (PIA, bottom row). These products highlight the structural changes in hydrometeor distribution and radar attenuation associated with the storm's intensification.

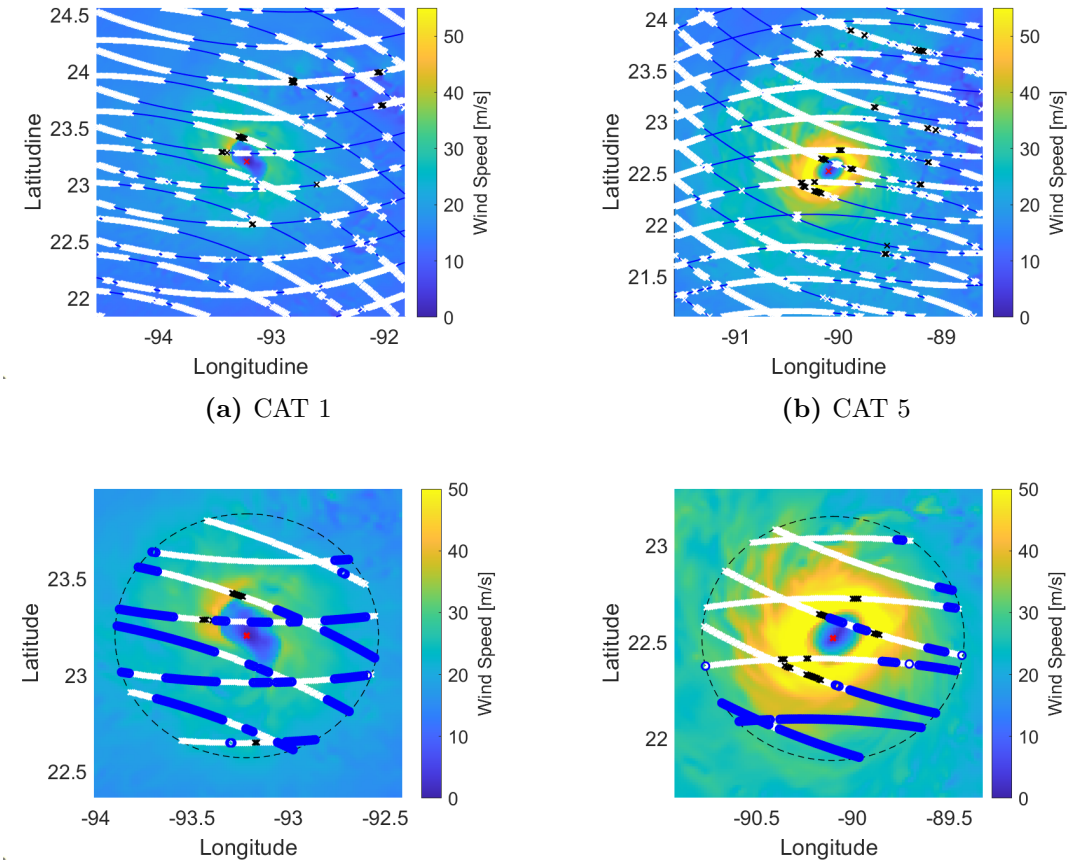

(a) CAT 1 **(b)** CAT 5

(c) CAT 1 **(d)** CAT 5

Figure 4.14: WIVERN antenna scan track and zoomed valid measurements at 2 km altitude across the core of Hurricane Milton before (CAT 1, left) and after (CAT 5, right) rapid intensification. Top: full track over wind speed background. Bottom: zoom within 70 km radius, showing valid Doppler points (blue), rejected for $Z < -18$ dBZ (white crosses) or $|w| > 2$ m/s (black crosses).

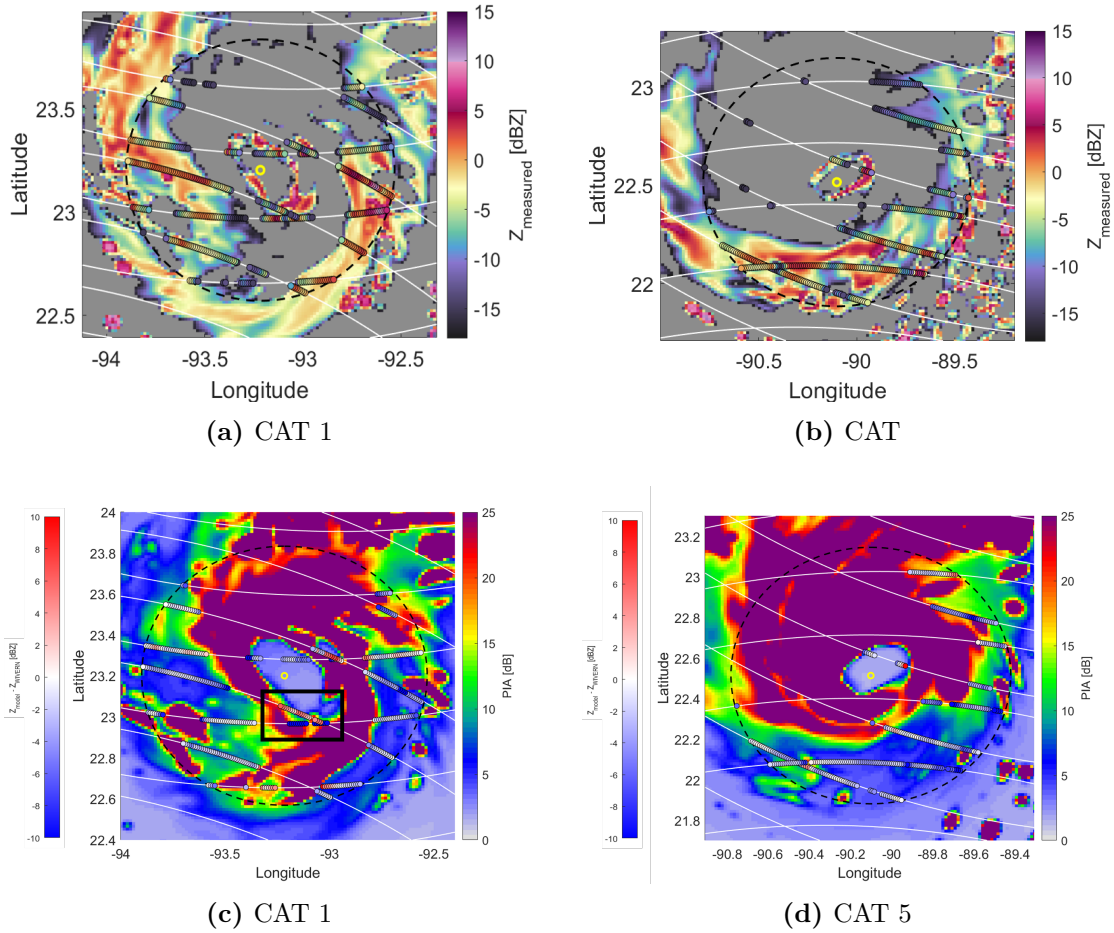

(a) CAT 1 **(b)** CAT **(c)** CAT 1 **(d)** CAT 5

Figure 4.15: WIVERN-simulated reflectivity (top) and path-integrated attenuation (PIA, bottom) across the core of Hurricane Milton at 2 km altitude. Left: Category 1 before rapid intensification. Right: Category 5 after intensification. Reflectivity (Z_{measured}) highlights convective structures, while PIA maps show signal attenuation due to hydrometeor loading.

The ability of WIVERN to observe Doppler velocities along slanted lines of sight proves particularly advantageous in detecting wind structures within highly attenuating regions. The geometry of the slant view plays a fundamental role not only in the wind retrievals but also in shaping the measured reflectivity field. This is especially evident in Figure 4.15c, where the reflectivity derived from the WIVERN simulator is compared to the model-simulated reflectivity obtained under simplified assumptions. In a first-order approach, attenuation is estimated by treating each atmospheric column as an isolated one-dimensional vertical profile. The PIA is computed by vertically integrating the extinction coefficient and subtracting

the result, scaled by the slant amplification factor $1/\cos(\theta_I) \approx 1.34$, from the unattenuated model reflectivity, yielding a first approximation of the attenuated reflectivity. However, this method does not account for the actual path followed by the radar beam as it propagates through the atmosphere. By contrast, the WIVERN simulator resolves the full three-dimensional propagation of the radar signal along its slanted path, properly modeling its interaction with the volume of hydrometeors it traverses. As a result, attenuation effects are captured more realistically. The differences between the model-derived and simulator-derived reflectivity fields become particularly relevant in regions with strong spatial variability in hydrometeor content, which translates into localized gradients in the PIA field. Figure 4.16 highlights this particular area where the slanted viewing geometry enables WIVERN to bypass strongly attenuating regions. A specific segment of the scanning track, marked with a black rectangle, demonstrates this phenomenon. Within this region, two contrasting scenarios emerge. In the first, indicated by red-colored points, the radar beam intersects the eyewall from above 2 km altitude, where strong attenuation significantly reduces the measured reflectivity compared to the model's 1D estimate. In the second scenario, represented by blue points, the radar beam penetrates from within the eye, where attenuation is weaker, and results in higher reflectivity values than predicted by the simplified model. These cases illustrate that WIVERN slant-view geometry is not inherently disadvantageous due to increased path length; on the contrary, in deep convective environments, it can provide access to low-level volumes otherwise hidden to conventional nadir-looking W-band radars.

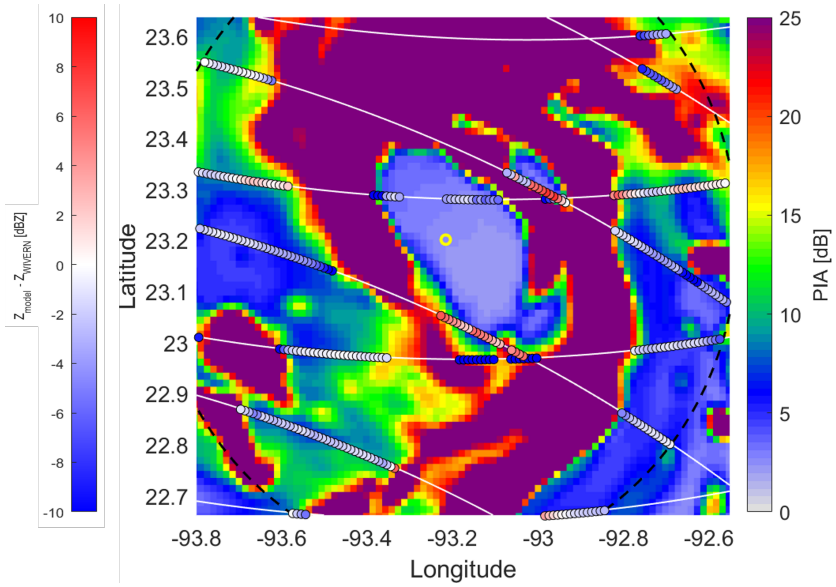

Figure 4.16: Zoomed-in view of the observation track segment highlighted in Figure 4.15c.

To perform the Holland model fitting using WIVERN Doppler observations, it is first necessary to project the tangential wind field onto the radar's LOS. This requires constructing two sets of unit vectors:

- $\mathbf{u}_{\text{wind}}$: the unit vector tangential to the storm circulation at each measurement location;
- $\mathbf{u}_{\text{ant}}$: the unit vector pointing from the satellite to the observed atmospheric volume, i.e., along the radar LOS.

The vectors $\mathbf{u}_{\text{ant}}$ were computed by converting the satellite and measurement geodetic coordinates to the Earth-Centered Earth-Fixed (ECEF) frame, and subsequently to the local East-North-Up (ENU) frame centered on the tropical cyclone. The direction vector from the satellite to each measurement point was then normalized in the horizontal plane to obtain $\mathbf{u}_{\text{ant}}$.

To compute $\mathbf{u}_{\text{wind}}$, the position of each observation point relative to the storm center was used to define the local azimuthal direction. A vertical unit vector was then used to compute the horizontal tangential component via a cross product, yielding vectors tangent to the approximated circular wind field.

Figure 4.17 illustrates these two vector fields superimposed on the background model wind field at 2 km altitude. The left panel shows the wind tangential vectors $\mathbf{u}_{\text{wind}}$, while the right panel displays the antenna LOS direction vectors $\mathbf{u}_{\text{ant}}$. Both are plotted at the locations of valid WIVERN measurements.

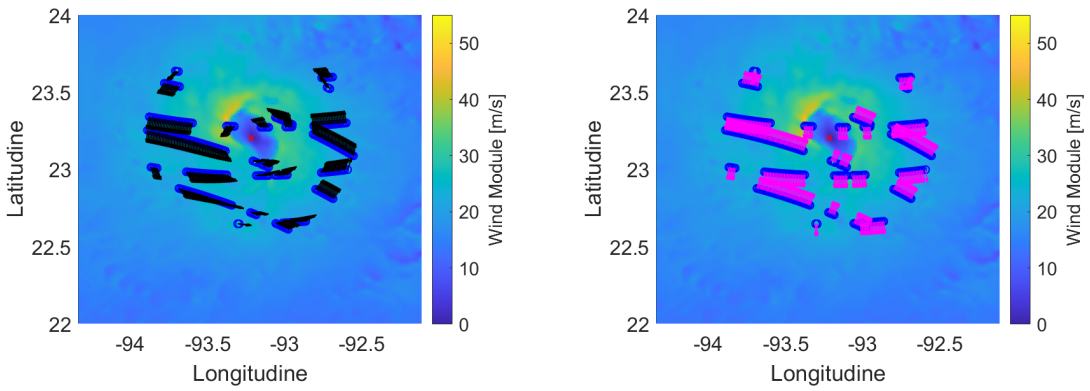

(a) Versors $\mathbf{u}_{\text{wind}}$.

(b) Versors $\mathbf{u}_{\text{ant}}$.

Figure 4.17: Direction vectors used to relate the Holland model to WIVERN line-of-sight Doppler measurements for the case of Milton CAT 1. Left: wind tangential unit vectors ($\mathbf{u}_{\text{wind}}$) derived from geodetic geometry and storm-relative motion. Right: antenna direction unit vectors ($\mathbf{u}_{\text{ant}}$) derived from satellite and LOS coordinates. Both are projected over the model wind field at 2 km altitude, with valid WIVERN observations marked in blue.

The optimization was performed using nonlinear least-squares techniques, directly fitting the Holland wind profile to the Doppler LOS measurements retrieved by WIVERN. Starting from the parameter estimates obtained from the model-based fit, the algorithm adjusted the shape parameter B, the radius of maximum wind RMW, and the pressure drop ΔP to best match the observed LOS velocities.

To enable the comparison, the theoretical tangential wind speed $V_{\tan}(r)$ was projected along the radar line-of-sight direction:

$$V_{\text{hlos}} = (\mathbf{u}_{\text{wind}} \cdot \mathbf{u}_{\text{ant}}) \cdot V_{\tan}(r),$$

where the dot product between the local wind direction and antenna pointing vector accounts for the slant-view geometry of WIVERN. The fitting procedure accounts for this geometry explicitly, allowing the model to reproduce the observed LOS Doppler shifts.

The results of the fit are summarized in Tables 4.3 end 4.4, and highlight WIVERN ability to reconstruct the radial structure of the tangential wind field despite the asymmetries present in the real storm.

Table 4.3: Fitted parameters of the Holland model at 2 km altitude during the Category 1 stage (07 October 2024, 00:00 UTC). Includes both model-derived and WIVERN-retrieved fits.

Method	**B**	**RMW** [km]	**ΔP** [Pa]
Initial guess (from J min)	1.50	25.00	1850.00
Nonlinear opt. (MODEL data, `lsqcurvefit`)	1.51	25.10	1847.07
Nonlinear opt. (WIVERN data, `lsqcurvefit`)	1.49	25.72	1803.14

Table 4.4: Fitted parameters of the Holland model at 2 km altitude during the Category 5 stage (08 October 2024, 00:00 UTC). Includes both model-derived and WIVERN-retrieved fits.

Method	**B**	**RMW** [km]	**ΔP** [Pa]
Initial guess (from J min)	2.00	20.00	4050.00
Nonlinear opt. (MODEL data, `lsqcurvefit`)	2.06	18.73	4226.85
Nonlinear opt. (WIVERN data, `lsqcurvefit`)	1.91	21.46	4326.04

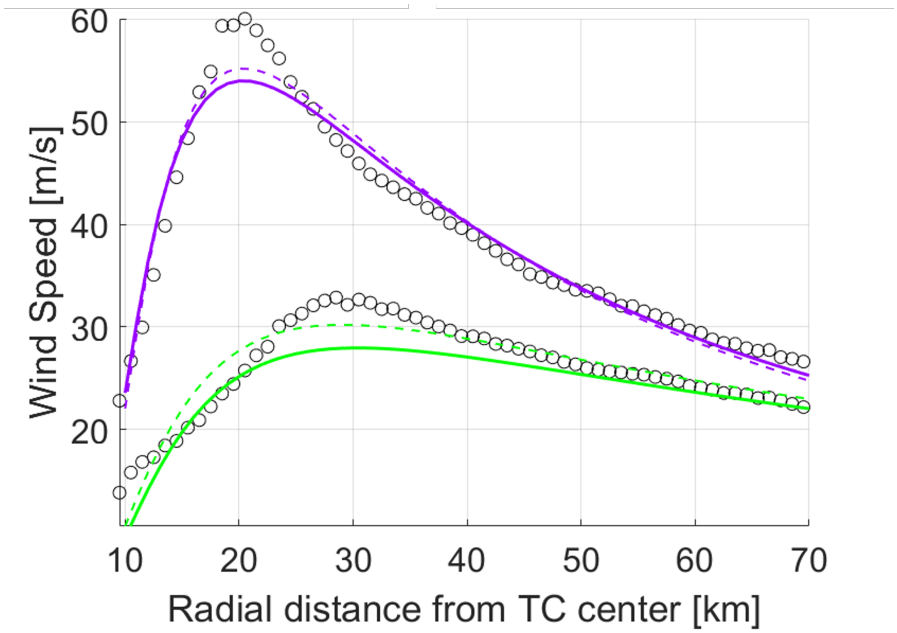

Figure 4.18: Azimuthally averaged wind profiles at 2 km altitude for Hurricane Milton before (Category 1, green lines) and after (Category 5, purple lines) the rapid intensification event. Dots represent the wind speed derived from model output, while dashed lines show the Holland fits to the model data. Solid lines indicate the Holland profiles fitted to the WIVERN-retrieved Doppler measurements. All curves are computed within a 70 km radius from the TC center.

Figure 4.18 illustrates the resulting radial profiles of horizontal wind speed at 2 km altitude. Dots represent the azimuthal average of wind speed computed from the model outputs, while dashed lines correspond to the Holland best-fit profiles for those data. The thick solid lines, on the other hand, show the profiles reconstructed by fitting the WIVERN Doppler measurements using the least-squares procedure described earlier. The results clearly demonstrate WIVERN ability to detect the substantial increase in wind speed, from about 30 m/s to over 60 m/s, that occurred within a 24-hour period. Despite the complexity of the inner-core environment and the challenges posed by signal attenuation, the retrieved profiles closely match the model-based fits, especially within the storm's inner 70 km. This confirms WIVERN potential to monitor the evolution of tropical cyclone wind structure, including the occurrence of rapid intensification. From an observational standpoint, the ability to revisit the same storm within a 12–24 hour window, thanks to the combination of ascending and descending orbits, represents a unique advantage of the WIVERN mission. In the case of Hurricane Milton, two overpasses were available within a 24-hour interval, enabling an accurate assessment of wind field evolution across the RI phase.

Conclusions

This thesis has investigated the potential of the WIVERN satellite mission to advance our capability to observe and understand TC dynamics, with a particular focus on internal wind structure and rapid intensification. Through the application of end-to-end simulations to a high-resolution WRF simulation of Hurricane Milton (2024), several key findings have emerged.

First, WIVERN Doppler-based wind retrieval system proves capable of reconstructing the three-dimensional cyclonic circulation across a wide range of altitudes. Despite limitations caused by attenuation and reflectivity gradients in the eye and convective towers, WIVERN is able to capture key features such as low-level inflow, upper-level outflow, and the structure of the eyewall.

Second, the mission's capability to resolve vertical wind shear and to detect asymmetric structures under shear conditions has been demonstrated. The analysis of quadrant-based wind fields shows that shear-induced asymmetries in the inner-core flow are preserved in the retrieved data, supporting the use of WIVERN for characterizing storm structure in realistic shear environments.

Third, WIVERN exhibits significant potential for monitoring the evolution of tropical cyclones. In the case of Hurricane Milton, the availability of two satellite overpasses within a 24-hour window enabled the identification of a doubling in maximum wind speed, consistent with rapid intensification. Holland model fits to WIVERN-retrieved wind profiles closely match those derived from model data, confirming the radar's ability to capture radial wind structure and intensity changes across the RI phase.

These results collectively suggest that WIVERN could fill critical gaps in the current global observing system by providing high-resolution, in-cloud wind observations at regular intervals. Such measurements are essential for improving our understanding of storm physics, validating numerical models, and potentially enhancing short-term forecasting of hazardous tropical systems.

Future work should explore data assimilation strategies to fully exploit WIVERN observations in operational weather prediction models and expand the analysis to a broader set of storm scenarios under varying environmental conditions.

Bibliography

[1] K. T. Bhatia, G. A. Vecchi, H. Murakami, J. P. Kossin, K. W. Dixon, and T. R. Knutson. «Projected Response of Tropical Cyclone Intensity and Intensification in a Global Climate Model». In: *Journal of Climate* 32.20 (2019), pp. 6051–6071. DOI: 10.1175/JCLI-D-18-0740.1 (cit. on p. 12).

[2] K. Emanuel. «Response of global tropical cyclone activity to increasing CO_2: Results from downscaling CMIP6 models». In: *Journal of Climate* 33.17 (2020), pp. 6651–6670. DOI: 10.1175/JCLI-D-20-0122.1 (cit. on p. 12).

[3] ESA. *Report for Mission Selection: Earth Explorer 11 Candidate Mission WIVERN*. Tech. rep. ESA-EOPSM-WIVE-RP-4798. 234 pages. Noordwijk, The Netherlands: European Space Agency, 2025. DOI: 10.5281/zenodo.15607041 (cit. on pp. 12, 20).

[4] F. Fabry. *Radar Meteorology: Principles and Practice*. Cambridge University Press, 2015. ISBN: 9780521688026 (cit. on pp. 15, 17, 19).

[5] A. Battaglia, P. Kollias, et al. «Spaceborne Cloud and Precipitation Radars: Status, Challenges, and Ways Forward». In: *Reviews of Geophysics* 58.3 (2020). e2019RG000686 10.1029/2019RG000686, e2019RG000686. DOI: 10.1029/2019RG000686. eprint: https://agupubs.onlinelibrary.wiley.com/doi/pdf/10.1029/2019RG000686. URL: https://agupubs.onlinelibrary.wiley.com/doi/abs/10.1029/2019RG000686 (cit. on p. 19).

[6] L. Ricciardulli et al. «Remote sensing and analysis of tropical cyclones: Current and emerging satellite sensors». In: *Remote Sensing* 15.3 (2023), p. 601. DOI: 10.3390/rs15030601 (cit. on p. 20).

[7] A. J. Illingworth, A. Battaglia, J. C. Nicol, S. Tanelli, F. Tridon, M. Wolde, et al. «WIVERN: A New Satellite Concept to Provide Global In-Cloud Winds, Precipitation and Cloud Properties». In: *Bulletin of the American Meteorological Society* 99.8 (2018), pp. 1587–1604. DOI: 10.1175/BAMS-D-16-0047.1 (cit. on pp. 20, 21, 23).

[8] A. Battaglia, P. Martire, É. Caubet, L. Phalippou, F. Stesina, P. Kollias, and A. J. Illingworth. «Observation Error Analysis for the Wind Velocity Radar Nephoscope W-band Doppler Conically Scanning Spaceborne Radar via End-to-End Simulations». In: *Atmospheric Measurement Techniques* 15 (2022), pp. 3011–3030. DOI: 10.5194/amt-15-3011-2022 (cit. on pp. 20–23, 25, 35).

[9] F. Tridon, A. Battaglia, A. Rizik, F. E. Scarsi, and A. J. Illingworth. «Filling the Gap of Wind Observations Inside Tropical Cyclones». In: *Earth and Space Science* 10 (2023). DOI: 10.1029/2023EA003099 (cit. on pp. 20, 22, 23, 25).

[10] A. Battaglia, Ali Rizik, Ishuwa Sikaneta, and Frederic Tridon. «I and Qs Simulation and Processing Envisaged for Spaceborne Polarization Diversity Doppler Radars». In: *IEEE Transactions on Geoscience and Remote Sensing* 63 (2025), pp. 1–14. DOI: 10.1109/TGRS.2025.3529672 (cit. on pp. 20, 22).

[11] Alessandro Battaglia, Cinzia Cambiotti, Anna Filomena Carbone, and Sergio Da Silva. «Reconstruction of the Horizontal Wind Field Inside Weather Systems from the Sparse Sampling Envisaged for the Wind Velocity Radar Nephoscope (WIVERN) Mission». In: *IGARSS 2024 - 2024 IEEE International Geoscience and Remote Sensing Symposium*. 2024, pp. 8925–8927. DOI: 10.1109/IGARSS53475.2024.10640420 (cit. on p. 21).

[12] S. L. E. F. da Silva, A. Battaglia, C. Cambiotti, and A. F. Carbone. «Sparse Sampling Reconstruction of Wind Fields for Space-Borne Doppler Radars». In: *Journal of LaTeX Class Files* XX.X (2025). Accepted for publication, pp. 1–14 (cit. on pp. 21, 37–40).

[13] A. Battaglia, M. Recupero, et al. «Peeping inside tropical cyclones with the WIVERN space-borne Doppler radar». In: *Earth and Space Science* (2025). under submission, available at https://wivern.polito.it/publications/ (cit. on pp. 21–24, 34, 37, 52).

[14] A. Battaglia, S. Tanelli, and P. Kollias. «Polarization Diversity for Millimeter Spaceborne Doppler Radars: An Answer for Observing Deep Convection?» In: *Journal of Atmospheric and Oceanic Technology* 30.12 (2013), pp. 2768–2787. DOI: 10.1175/JTECH-D-13-00085.1 (cit. on p. 22).

[15] M. Wolde, A. Battaglia, C. Nguyen, A. L. Pazmany, and A. Illingworth. «Implementation of polarization diversity pulse-pair technique using airborne W-band radar». In: *Atmospheric Measurement Techniques* 12.1 (2019). DOI: 10.5194/amt-12-253-2019 (cit. on p. 22).

[16] A. Battaglia and G. Panegrossi. «What Can We Learn from the CloudSat Radiometric Mode Observations of Snowfall over the Ice-Free Ocean?» In: *Remote Sensing* 12.20 (2020). ISSN: 2072-4292. DOI: 10.3390/rs12203285. URL: https://www.mdpi.com/2072-4292/12/20/3285 (cit. on p. 22).

[17] F. E. Scarsi, A. Battaglia, F. Tridon, P. Martire, R. Dhillon, and A. Illingworth. «Mispointing correction methods for the conically scanning WIVERN Doppler radar». In: *Atmospheric Measurement Techniques Discussions* (2023), pp. 1–26. DOI: 10.5194/amt-2023-117 (cit. on p. 22).

[18] Francesco Manconi, Paolo Martire, Fabrizio Stesina, and Alessandro Battaglia. «High accuracy attitude determination of a spacecraft with a fast-rotating Doppler radar reflector». In: *Acta Astronautica* 233 (2025), pp. 66–81. ISSN: 0094-5765. DOI: https://doi.org/10.1016/j.actaastro.2025.03.026. URL: https://www.sciencedirect.com/science/article/pii/S0094576525001821 (cit. on p. 22).

[19] A. Battaglia, R. Dhillon, and A. J. Illingworth. «Doppler W-band Polarization Diversity Space-borne Radar Simulator for Wind Studies». In: *Atmospheric Measurement Techniques* 11 (2018), pp. 5965–5979. DOI: 10.5194/amt-11-5965-2018 (cit. on p. 22).

[20] M. Coppola, A. Battaglia, F. Tridon, and P. Kollias. «Improved hydrometeor detection near the Earth's surface by a conically scanning spaceborne W-band radar». In: *EGUsphere* 2025 (2025), pp. 1–24. DOI: 10.5194/egusphere-2025-416. URL: https://egusphere.copernicus.org/preprints/2025/egusphere-2025-416/ (cit. on p. 22).

[21] A. Battaglia, F. E. Scarsi, K. Mroz, and A. Illingworth. «In-orbit cross-calibration of millimeter conically scanning spaceborne radars». In: *Atmospheric Measurement Techniques* 16.12 (2023). DOI: 10.5194/amt-16-3283-2023 (cit. on p. 22).

[22] Nicolas Sasso et al. «Impact of WIVERN Wind Observations on ARPEGE Numerical Weather Prediction Model Forecasts Using an Ensemble of Data Assimilation Method». In: *Quarterly Journal of the Royal Meteorological Society* n/a.n/a (), e4991. DOI: https://doi.org/10.1002/qj.4991. eprint: https://rmets.onlinelibrary.wiley.com/doi/pdf/10.1002/qj.4991. URL: https://rmets.onlinelibrary.wiley.com/doi/abs/10.1002/qj.4991 (cit. on p. 23).

[23] R. A. Houze. «Clouds in Tropical Cyclones». In: *Monthly Weather Review* 138.2 (2010), pp. 293–344. DOI: 10.1175/2009MWR2989.1 (cit. on pp. 26, 29, 31, 32, 51).

[24] S. Pappas. *Astronaut's Photos of Hurricane Florence From the International Space Station*. Accessed: 2025-07-11. 2018. URL: https://www.sciencealert.com/astronauts-photos-of-hurricane-florence-from-international-space-station (cit. on pp. 26, 27).

[25] National Hurricane Center. *Saffir–Simpson Hurricane Wind Scale*. Accessed: 14 July 2025. 2023. URL: https://www.nhc.noaa.gov/aboutsshws.php (cit. on p. 30).

[26] K. R. Fox and F. Judt. «A Numerical Study on the Extreme Intensification of Hurricane Patricia (2015)». In: *Weather and Forecasting* 33.4 (2018), pp. 989–999. DOI: 10.1175/WAF-D-17-0101.1 (cit. on p. 32).

[27] R. F. Rogers, S. Aberson, M. M. Bell, D. J. Cecil, J. D. Doyle, T. B. Kimberlain, J. Morgerman, L. K. Shay, and C. Velden. «Re-writing the tropical record books: The extraordinary intensification of Hurricane Patricia (2015)». In: *Bulletin of the American Meteorological Society* 98.10 (2017), pp. 2091–2112. DOI: 10.1175/BAMS-D-16-0039.1 (cit. on p. 32).

[28] T. B. Kimberlain, E. S. Blake, and J. P. Cangialosi. *Tropical Cyclone Report: Hurricane Patricia (EP202015)*. Tech. rep. NHC Tropical Cyclone Report. National Hurricane Center, Feb. 2016. URL: https://www.nhc.noaa.gov/data/tcr/EP202015_Patricia.pdf (cit. on pp. 32, 33).

[29] J. G. Powers et al. «The Weather Research and Forecasting (WRF) Model: Overview, System Efforts, and Future Directions». In: *Bulletin of the American Meteorological Society* 98.8 (2017), pp. 1717–1737. DOI: 10.1175/BAMS-D-15-00308.1 (cit. on p. 35).

[30] W. C. Skamarock, J. B. Klemp, M. G. Duda, L. D. Fowler, S. H. Park, and T. D. Ringler. *A Description of the Advanced Research WRF Model Version 4*. Tech. rep. National Center for Atmospheric Research (NCAR) Technical Note NCAR/TN-556+STR, 2019. DOI: 10.5065/1DFH-6P97 (cit. on p. 35).

[31] John L. Beven II, Laura Alaka, and Cody Fritz. *Tropical Cyclone Report: Hurricane Milton (AL142024)*. Tech. rep. 5–10 October 2024. National Hurricane Center, Mar. 2025. URL: https://www.nhc.noaa.gov/data/tcr/AL142024_Milton.pdf (cit. on p. 36).

[32] M. T. Montgomery et al. «The Role of the Boundary Layer in Hurricane Eyewall Replacement Cycles». In: *Journal of the Atmospheric Sciences* 63 (2006), pp. 2080–2095 (cit. on p. 48).

[33] W. M. Frank and E. A. Ritchie. «Effects of Vertical Wind Shear on Hurricane Intensity and Structure». In: *Monthly Weather Review* 129.10 (2001), pp. 2249–2269. DOI: 10.1175/1520-0493(2001)129<2249:EOVWSO>2.0.CO;2 (cit. on p. 51).

[34] R. F. Rogers, P. D. Reasor, and J. Zhang. «Multiscale Structure and Evolution of Hurricane Earl (2010) during Rapid Intensification». In: *Monthly Weather Review* 141.11 (2013), pp. 4193–4212. DOI: 10.1175/MWR-D-12-00334.1 (cit. on pp. 51, 52).

[35] M. Wu, K. Yeung, and W. Chang. «Trends in Western North Pacific Tropical Cyclone Intensity». In: *Eos, Transactions American Geophysical Union* 87 (2016). DOI: 10.1029/2015EO020181 (cit. on p. 51).

[36] J. C. DeHart, R. A. Jr. Houze, and R. F. Rogers. «Quadrant Distribution of Tropical Cyclone Inner-Core Kinematics in Relation to Environmental Shear». In: *Journal of the Atmospheric Sciences* 71.7 (2014), pp. 2713–2732. DOI: 10.1175/JAS-D-13-0298.1 (cit. on p. 51).

[37] C. J. Matyas. «Locating Convection in Landfalling Tropical Cyclones: A GIS-Based Analysis of Radar Reflectivities and Comparison to Lightning-Based Observations». In: *Physical Geography* 31.5 (2010), pp. 385–406. DOI: 10.2747/0272-3646.31.5.385 (cit. on p. 52).

[38] G. J. Holland. «An Analytic Model of the Wind and Pressure Profiles in Hurricanes». In: *Monthly Weather Review* 108.8 (1980), pp. 1212–1218 (cit. on pp. 56, 58).